

Postgraduate Master Program “Optics and Vision”

University of Crete



Development of an advanced system for in-vivo Mouse Optical Neuro-imaging Applications

by

Marsida Bekollari

Supervising Professor:

*Dimitrios Papazoglou
(Assistant Professor, University of Crete)*

Supervising Researchers:

*Athanasios D. Zacharopoulos
(Research Fellow, FORTH-IESL)*

*Giannis Zacharakis
(Senior Research Scientist, FORTH-IESL)*

Evaluation committee:

*Dimitrios Papazoglou
(Assistant Professor, University of Crete)*

*Maria Kafesaki
(Associate Professor, University of Crete)*

*Vangelis Sakkalis
(Principal Researcher, FORTH-ICS)*

Heraklion, February 2015

Postgraduate Master Program “Optics and Vision”

University of Crete



Project Title

“Development of an advanced system for in-vivo Mouse Optical Neuro-imaging
Applications”

by

Marsida Bekollari

This study was submitted as part of the obligations for the conferment of the Master in
Science certification of the MSc Program “Optics and Vision” and was presented at the
three-member evaluation committee constituted by:

Dimitrios Papazoglou
(Assistant Professor, University of Crete)

Maria Kafesaki
(Associate Professor, University of Crete)

Vangelis Sakkalis
(Principal Researcher, FORTH-ICS)

Heraklion, February 2015

Abstract

Fluorescence Molecular Tomography (FMT) is an inexpensive, noninvasive, fast, three-dimensional (3D), *in vivo* optical imaging modality that has been well established in providing quantitative imaging of the distribution of fluorescence targets. This translates to information about gene expression and molecular function, in small animals and biological tissues where the transmission of light is diffusive. The recovery of this distribution in a tomographic fashion requires a model-based reconstruction and depends on an appropriate mathematical model that describes light propagation in tissue (forward model) and the solution of an image reconstruction algorithm (inverse problem) based on the forward. The highly diffusive nature of biological tissue leads to a challenging (ill-posed) inverse problem and effectively limits the resolution and the quantification accuracy achieved. A solution to these problems can be found by including *a priori* known information to the inversion that can improve the accuracy of the photon propagation (forward) model and restrict the inversion procedure to meaningful solutions, that is, to reduce the uncertainty of the inverse problem. The information could be for example, the distributions of optical parameters (absorption, scattering) in the relevant wavelengths through the tissue under investigation and an accurate geometric description of its boundaries.

Purpose

The aim of this project is to optimize the FMT imaging system, by adding prior information to the inversion procedure. This will be done by accessing two aspects of the problem. The first will be the recovery of the absorption and scattering distributions over the domain of the mouse and the second is the development of a profilometry device or 3D scanning procedure, to be included in the FMT apparatus, to acquire information on the shape of the mouse's boundary.

Methods

To investigate the effect of optical properties, such as absorption and scattering, in the reconstruction problem in Diffuse Optical Tomography (DOT), we are going to use resin made phantoms with varying optical properties. To determine the optical characteristics of the materials used to fabricate the phantoms we employ Spectrophotometer measurements of Diffuse Reflectance and Diffuse Transmittance. From those we can then calculate the absorption and scattering parameters of the materials, by using the Kubelka-Munk model, according to the relevant literature. Since our main interest is neuro-imaging the specimens

used in this work represent separately the optical properties of the different tissue types of the mouse's head. Following, a procedure that would allow the estimation of the absorption and scattering distributions through the media by using the FMT apparatus and measurements, based on the Diffusion Equation, was attempted with the employment of a simple inversion solution. Simultaneously, a 3D shape extraction mechanism was fashioned to augment the existing FMT apparatus with the ability to obtain the surface scan of the samples under imaging.

Results

The results of the project consist of three parts. The first part includes the fabrication of specimens and the determination of their optical properties using a Spectrophotometer. In the second part a simple inversion from FMT measurements on the specimens is performed by using the simulation of the light propagation (forward). Finally, in the third part a 3D scanning procedure is presented in order to be used in 3D surface reconstruction.

Conclusions

Using prior information can be the solution to the problems arising from the highly diffusive nature of biological tissue and the ill-posedness of the inversion involved in the image reconstruction. We have demonstrated ways to create this prior information, using the existing FMT setup.

Η μοριακή τομογραφία φθορισμού (FMT) είναι μια φθηνή, μη-επεμβατική, γρήγορη, τρισδιάστατη μέθοδος έμβιας οπτικής απεικόνισης που μπορεί να παρέχει ποσοτική απεικόνιση της κατανομής του φθορίζοντων στόχων. Κάτι που μεταφράζεται σε πληροφορία για την έκφραση γονιδίων και τη μοριακή λειτουργία, σε μικρά ζώα και βιολογικούς ιστούς όπου η διάδοση του φωτός είναι διάχυτη. Γι' αυτό το λόγο, η τομογραφική ανάκτηση αυτής της κατανομής βασίζεται στην μαθηματική ανακατασκευή εικόνας και εξαρτάται από ένα κατάλληλο μαθηματικό μοντέλο που να περιγράφει τη διάδοση του φωτός στον ιστό (Forward Model) καθώς και από τον αλγόριθμο ανακατασκευής της εικόνας (Inverse Model). Η ιδιαίτερα διάχυτη φύση του βιολογικού ιστού οριοθετεί τις δυνατότητες του μαθηματικού μοντέλου με αποτέλεσμα να περιορίζει την ανάλυση και την ακρίβεια προσδιορισμού της ποσοτικοποίησης. Λύση στο πρόβλημα μπορεί να δώσει η προσθήκη πληροφορίας και γνωστών στοιχείων (priority known information) στην διαδικασία της απεικόνισης και να βελτιώσει έτσι την ακρίβεια στο μοντέλο διάδοσης του φωτός καθώς και την διαδικασία ανακατασκευής. Αυτές οι πληροφορίες θα μπορούσαν να είναι ο ακριβής προσδιορισμός των οπτικών παραμέτρων (απορρόφηση, σκέδαση) του ιστού στα σχετικά μήκη κύματος και μια ακριβή γεωμετρική περιγραφή του δεδομένου δείγματος προς εξέταση.

Σκοπός

Ο στόχος αυτής της εργασίας είναι η βελτιστοποίηση της απεικόνισης της μοριακής τομογραφίας φθορισμού (FMT), με την προσθήκη πληροφοριών (priority known information) στη διαδικασία αντιστροφής. Αυτό πραγματοποιείται ορίζοντας δυο πτυχές του προβλήματος. Η πρώτη είναι η ανάκτηση των συντελεστών απορρόφησης και σκέδασης στην περιοχή του σώματος του ποντικού και η δεύτερη είναι η ανάπτυξη μιας συσκευής προφίλομετρίας ή μιας διαδικασίας σάρωσης με σκοπό την ανακατασκευή του σχήματος του ποντικού. Το πρωτότυπο θα ενσωματωθεί στο σύστημα του FMT.

Μέθοδοι

Για να μελετήσουμε την επιρροή των οπτικών ιδιοτήτων, όπως απορρόφηση και σκέδαση, στο πρόβλημα της ανακατασκευής στην διάχυτη οπτική τομογραφία (DOT), προετοιμάστηκαν ειδικά δείγματα τεχνητού ιστού ρητίνης με διαφορετικές τιμές οπτικών ιδιοτήτων. Για να μπορέσουμε να προσδιορίσουμε τα οπτικές ιδιότητες των υλικών πραγματοποιήθηκαν

μετρήσεις σε φασματοφωτόμετρο όπου λαμβάνουμε παραμέτρους όπως η διάχυτη ανάκλαση και η διάχυτη διάδοση του φωτός μέσα από αυτά τα υλικά. Από αυτά μπορούμε να προσδιορίσουμε τις οπτικές ιδιότητες εφαρμόζοντας το μαθηματικό μοντέλο Kubelka-Munk, σύμφωνα με την βιβλιογραφία. Εφόσον το ενδιαφέρον μας επικεντρώνεται στην νευροαπεικόνιση, τα δείγματά μας αντιπροσωπεύουν ιστούς που αφορούν στον εγκέφαλο του ποντικού. Στη συνέχεια, χρησιμοποιήθηκε μια διαδικασία εκτίμησης της κατανομής των συντελεστών απορρόφησης και σκέδασης στο μέσον χρησιμοποιώντας μετρήσεις από το σύστημα FMT, η οποία βασίζεται στην εξίσωση διάχυσης (Diffusion Equation), ακολουθώντας μια απλή μέθοδο αντιστροφής (inversion solution). Συγχρόνως, εγκαταστάθηκε μιας διαδικασία σάρωσης με laser με σκοπό την τρισδιάστατη ανακατασκευή του σχήματος του υπό εξέταση δείγματος.

Αποτελέσματα

Τα αποτελέσματα της συγκεκριμένης εργασίας χωρίζονται σε τρία (3) μέρη. Στο πρώτο μέρος παρουσιάζονται τα δείγματα που αντιπροσωπεύουν τους ιστούς του κεφαλιού του ποντικού, καθώς και ο προσδιορισμός των οπτικών ιδιοτήτων χρησιμοποιώντας φασματοφωτόμετρο. Στο δεύτερο μέρος παρουσιάζεται η λύση ενός απλού αντίστροφου προβλήματος από μετρήσεις από το FMT εφαρμόζοντας την εξίσωση διάχυσης. Τέλος, στο τρίτο μέρος παρουσιάζεται η διαδικασία σάρωσης με laser προκειμένου να χρησιμοποιηθεί στην τρισδιάστατη ανακατασκευή του σχήματος του ποντικού.

Συμπεράσματα

Τα αποτελέσματά μας δείχνουν ότι η προσθήκη πληροφοριών (prior information) στην διαδικασία της απεικόνισης μπορεί να αποτελέσει την λύση στα προβλήματα που προκαλεί η διάχυτη διάδοση του φωτός μέσα από τους ιστούς. Σε αυτήν την εργασία δείχνουμε μερικούς τρόπους προσδιορισμού αυτών των πληροφοριών (prior information), χρησιμοποιώντας το υπάρχων σύστημα Μοριακής Τομογραφίας Φθορισμού (FMT).

Dedicated to all those who inspire me
to be a better person every day...

Acknowledgements

All the measurements and the experiments for this study have been performed at “In-vivo Optical Imaging Lab” in the Institute of Electronic Structure & Laser of the Foundation for Research and Technology Hellas (FORTH).

This thesis would not have been possible without the great attitude and support of my supervisors. They always were helpful during the writing and the organization of the experiments. Their guidance at critical points has been extremely valuable for the completion of this study. Also, a great thanks to all the member of the lab for their help and moral support during the difficulties of the work. A special thanks goes to Stella Avtzi, for giving me all the appropriate information from her work in order to achieve some parts of my project.

This work was funded by the Grants “Skin-DOCTOR” and “Neureka!” implemented under the “Excellence” and “Supporting Postdoctoral Researchers” Actions respectively, of the “OPERATIONAL PROGRAMME EDUCATION AND LIFELONG LEARNING”, co-funded by the European Social Fund (ESF) and National Resources.

Finally, special thanks go out to my family and all my dear friends who stand me all these years.

Abstract	3
Περίληψη	5
Acknowledgements	8
Contents.....	9
Part A. Theory Background	
Introduction.....	12
Chapter 1	
1.1 What is Optical Imaging?.....	13
1.2 Diffuse Optical Tomography (DOT).....	15
1.3 Fluorescence Molecular Tomography (FMT).....	16
1.4 Significant parameters for Fluorescence Molecular Imaging.....	16
1.4.1 Interaction of light with biological tissues.....	17
1.4.2 Tissue Absorption and absorption coefficient μ_a	19
1.4.3 Scattering in tissue and Scattering coefficient μ_s	20
1.4.4 Total Attenuation coefficient μ_t	23
Chapter 2	
2.1 Photon transport models based on Radiative Transfer Equation (RTE)	24
2.1.1 Diffusion Theory and its approximation for Optical/Fluorescence Molecular Imaging.....	24
2.1.2 Boundary Condition and Source Terms.....	26
2.2 Overview of the Tomographic Imaging Reconstruction Problem.....	27
2.2.1 The Forward Model.....	28
2.2.2 Computational method-The Finite Element Method (FEM).....	28
2.2.3 The Inverse Model.....	29
2.3 Imaging Package tools for DOT in Matlab.....	30
Chapter 3	
3.1 Introduction in 3D Scanning Technology.....	33
3.2 The basic principle of laser triangulation.....	34
3.3 Camera Calibration.....	35

Part B. Experiments and Results

Chapter 4

Materials, Phantoms, Tools and Methods.....	40
<u>4.1</u> Determination of optical properties of phantom's materials.....	40
<u>4.2</u> Description of the propagation of light inside the media and experimental procedure in FMT system.....	45
<u>4.3</u> Information on the shape of the sample's boundary (3D scanning procedure).....	47

Chapter 5

Results.....	52
<u>5.1</u> Determination of optical characteristics of the material of the specimens used.....	53
<u>5.2</u> Simulation of the propagation of the light inside the media and determination of the optical properties (μ_a, μ_s) using diffusion approximation.....	58
<u>5.3</u> Scanning procedure for the 3D shape reconstruction of the sample.....	65

Chapter 6

<u>6.1</u> Conclusion	76
<u>6.2</u> Future Work.....	76

Chapter 7

<u>7.1</u> References.....	77
--	----

Part A. Theory Background

This essay will deal with optical imaging and in particular Fluorescence Molecular Tomography. This method of in-vivo optical imaging is nowadays widely used for preclinical molecular imaging. It is an emerging technology with great potential for improving prevention, diagnosis, and treatment of diseases. The term molecular imaging can be defined as the *in vivo* characterization and measurement of biologic processes at the cellular and molecular level. In order to improve this diagnostic method, which is based in the reconstruction of fluorescence distributions inside the biological tissue, there are some significant parameters which should be taken into account. The light interaction with tissues is important to be described in order to understand the parameters that affect the imaging. Such interaction can be the absorption, scattering, reflection or the fluorescence itself. An important tool to describe how light is propagated inside turbid tissue is the Diffusion Equation and its solution will be used to define what we call the forward model. To determine the parameters (absorption and scattering coefficients) related to the light interaction with tissue the inverse model is needed. A solution to describe properly the propagation is to give some (prior) information about the sample under investigation. Such information can be the optical properties of the media and the shape of the sample. The shape can be reconstructed using a 3D scanning procedure [1],[2].

1.1 What is Optical Imaging?

Optical imaging is a non-invasive method and it is based on the fact that photons travel through biological tissues and can be detected by ultrasensitive optical imaging systems. If the wavelength of this radiation is in the **400nm-780nm** range, we then have **visible** light (fig. 1). Optical imaging techniques rely on either intrinsic parameters such as absorption and scattering or refractive index or to specific targets such as luciferase, fluorescent proteins, fluorescent dyes to create contrast. Genes encoding luciferase and fluorescent proteins can be engineered into cells (e.g., cancer cell lines and infectious disease agents) and animals (transgenic mice and rats) to enable them to produce signal that can then be transmitted through biological tissue [3, 4]. Nevertheless, there are some issues with using light to probe tissue, light is heavily absorbed and scattered from biological tissue. The main absorbers in tissue are water and blood, with the defining components of the latter being hemoglobin and deoxyhemoglobin (fig. 5). In the figure it is shown that the absorption is minimal in the near infrared (NIR) region but even then, tissue penetration can only reach up to few centimeters. For that reason imaging with visible light is limited to small animal imaging or clinical applications such as in breast imaging[5], where the tissue thickness is small or the tissue absorption is relatively low. Equally important issue with using light to probe tissue is that it is strongly scattered. In fact, the effect of scattering is so strong that the description of light propagation in tissue should be approximated as for example with a diffusive propagation[6]. In Table 1.1 there is a comparison between diagnostic modalities using several criteria that are important for the diagnosis.

Reasons for optical imaging of biological tissue include [7]:

1. Optical photons provide non-ionizing and safe radiation for medical applications.
2. Optical spectra are based on absorption, fluorescence, or Raman scattering which provide biochemical information because they are related to the molecular conformation.
3. Optical absorption, in particular, reveals angiogenesis and hyper-metabolism, both of which are hallmarks of cancer, the former is related to the concentration of hemoglobin and the latter, to the oxygen saturation of hemoglobin. Therefore, optical absorption provides contrast for functional imaging.

4. Optical scattering spectra provide information about the size distribution of optical scatterers, such as cell nuclei.
5. Optical properties of targeted contrast agents provide contrast for the molecular imaging of biomarkers.
6. Optical properties or bioluminescence of products from gene expression provide contrast for the molecular imaging of gene activities.
7. Optical spectroscopy permits simultaneous detection of multiple contrast agents.

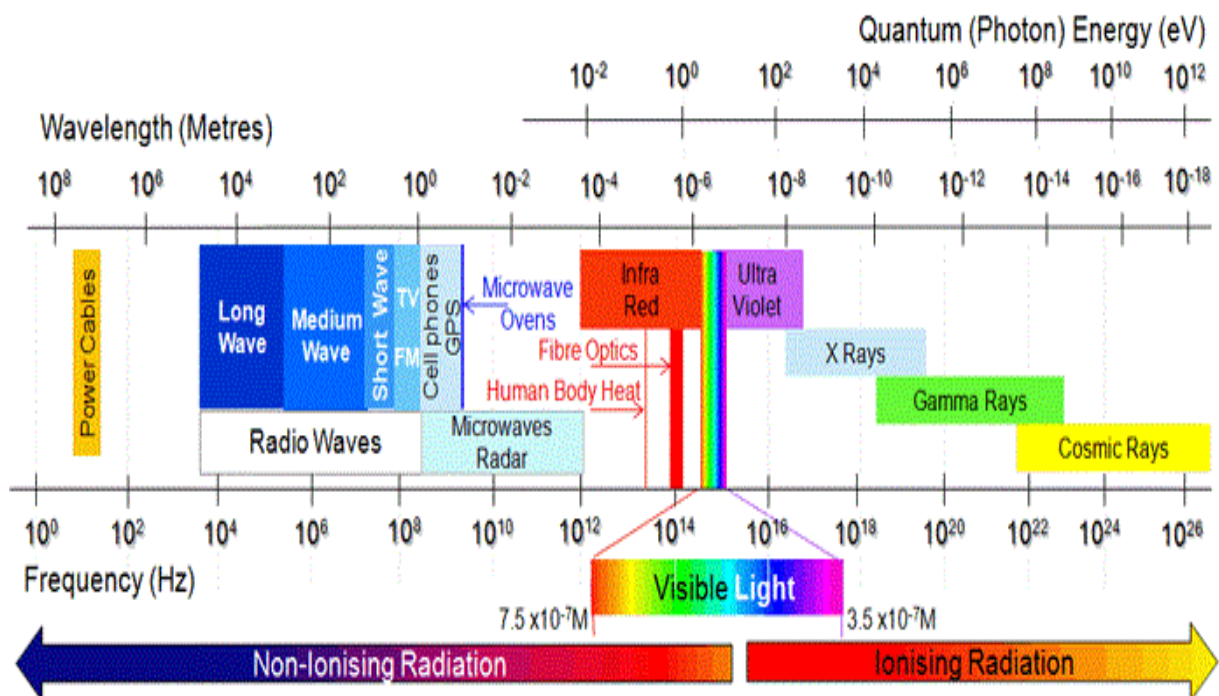


Figure 1: Electromagnetic Radiation Spectrum [47]

Characteristics	X-Ray Imaging	US	MRI	Optical Imaging
Soft-tissue contrast	<i>Poor</i>	<i>Good</i>	<i>Excellent</i>	<i>Excellent</i>
Spatial resolution	<i>Excellent</i>	<i>Good</i>	<i>Good</i>	<i>Mixed*</i>
Maximum imaging depth	<i>Excellent</i>	<i>Good</i>	<i>Excellent</i>	<i>Good</i>
Function	<i>None</i>	<i>Good</i>	<i>Excellent</i>	<i>Excellent</i>
Non-ionizing radiation	<i>no</i>	<i>Yes</i>	<i>Yes</i>	<i>Yes</i>
Data acquisition	<i>Fast</i>	<i>Fast</i>	<i>Slow</i>	<i>Fast</i>
Cost	<i>Low</i>	<i>Low</i>	<i>High</i>	<i>Low</i>

Table 1: Comparison of Various Medical Imaging Modalities.* High in ballistic imaging and photoacoustic tomography, low in diffuse optical tomography[8-10].

1.2 Diffuse Optical Tomography (DOT)

Diffuse optical tomography (DOT) is emerging as a viable new biomedical imaging modality. Using near-infrared (NIR) light, this technique recovers absorption as well as scattering properties of biological tissues. Currently, the main applications are brain, breast, limb, joint imaging. DOT provides access to a variety of physiological parameters that otherwise are not accessible, including imaging of hemodynamics and other fast-changing processes. This technology is based on delivering low-energy electromagnetic radiation, to one or more locations on the surface of the body part under investigation and measuring transmitted and/or back-reflected intensities at distances up to 10 cm [46]. The propagation of light in biomedical tissue is governed by the spatially varying scattering and absorption properties of the medium, which are described in the framework of scattering and absorption coefficients (μ_s and μ_a) or reduced or transport scattering coefficient (μ'_s). These coefficients are described in the following paragraphs. Differences in the refractive index between intracellular and extracellular fluids and

various subcellular components such as mitochondria or nuclei, as well as varying tissue densities, give rise to differences in scattering coefficient. Differences in chromophore content and concentration lead to different absorption coefficients. Based on measurements of transmitted and reflected light intensities on the surface of the medium, a reconstruction of the spatial distribution of the optical properties inside the medium is attempted [46].

1.3 Fluorescence Molecular Tomography (FMT)

An important tool for molecular imaging, fluorescence molecular tomography (FMT) is applied to recover the distribution of fluorescence reporters associated with cellular functions. In comparison with other molecular imaging approaches, fluorescence molecular imaging can obtain high sensitivity detection with low instrumentation expense. Such an imaging mode has attracted great attention due to the great availability of fluorescent proteins, dyes and probes that enable the non-invasive study of gene expression, protein function, protein-protein interactions and a large number of cellular processes. The application of fluorescence tomography would also help bioengineering scientists investigate disease processes, evaluate therapy response and develop new drugs. Opening new pathways for the characterization of biological processes in living animals at cellular and molecular levels, fluorescence tomography is currently applied for in vivo small animal imaging. In preclinical research, FMT is an attractive alternative to PET, as provides quantitative molecular information with non-ionizing radiation and stable probes [11]. In the next chapters, the fundamental principles, the experimental apparatus and the reconstruction algorithms are described.

1.4 Significant parameters for Fluorescence Molecular Tomography

In considering the potential use of in vivo fluorescence imaging in biological studies, there are some important parameters that should be taken into account in order to improve and to overcome intrinsic limitations that affect this imaging method. These limitations are related to the interaction of light with the tissue.

1.4.1 Interactions of Light with Biological Tissues

To understand the various modalities of light-tissue interaction, it is necessary to comprehend how photons penetrate biological tissue[2]. Most of biological tissues are characterized by optical scattering, absorption and reflection which is a consequence of light interaction with matter. A classical picture of these interactions is shown in Fig 2[12]. This behaviour of light in biological tissue presents a key challenge for optical imaging. Absorption takes place when a photon causes the elevation of an electron of a molecule from the ground state to an excited state (S_2), which is termed *excitation*. The excited electron may relax to the ground state (S_0) and send out *luminescence* (another photon) or heat. If another photon is produced then that emission is called *fluorescence* or *phosphorescence*, depending on the time of the excited electron spends in the excited state before returning to the ground state. These electronic transitions between ground states and excited states are described by the Jablonski energy diagram which is shown in Fig. 3. On this particular diagram, as a result of absorption, the electron occupies the S_2 orbital. There are different options that the electron releases the excess energy. It could happen through radiation less transitions or through emission of light quanta. In the term of radiation fewer transitions are included vibrational relaxation, internal conversion, intersystem crossing, and more. If there are vibrational levels of nearly equal energy that correspond to different electron levels, it is possible for the electron to switch from S_2 to S_1 . This process is known as internal conversion. No energy is emitted.

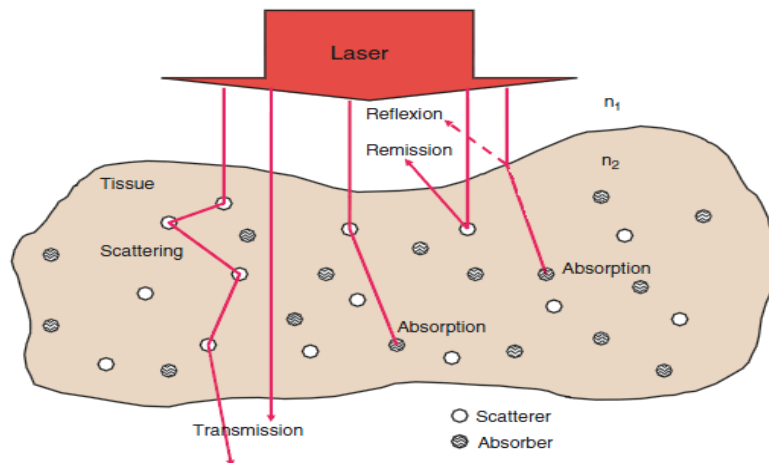


Figure 2: Optical behavior of a tissue layer during irradiation with laser light.

As the electron now occupies an excited vibrational level of S_1 , it can relax further to the ground vibrational level of this state. From there, it is finally possible for the electron to return to the ground electron state S_0 .

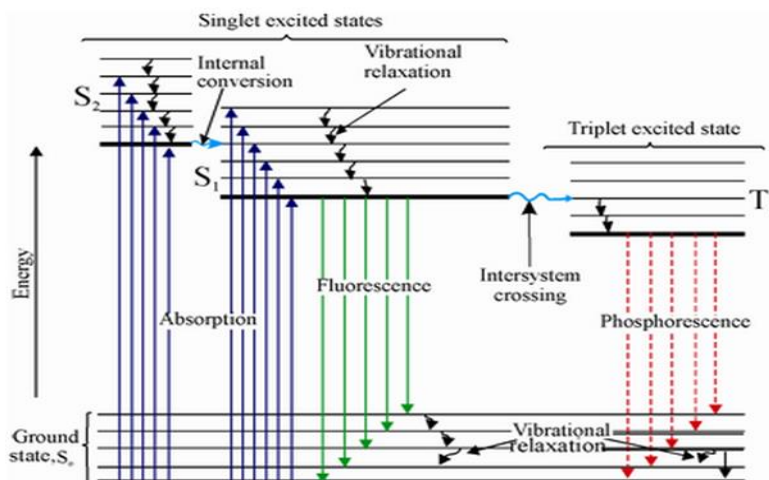


Figure 3: Jablonski energy diagram showing excitation and various possible mechanisms [48].

The process of emission is so called fluorescence. Similar to internal conversion is the process of intersystem crossing. The only difference is that the electron makes a transition from a singlet to a triplet state. The relaxation from an excited triplet state T_1 to the ground singlet state S_0 is so called phosphorescence. Due to these vibrational relaxation and the energy loss in the above processes, the radiated photon has lower energy than the excitation photon and this create a shift in the emission wavelength to higher values, the so called 'Stokes shift' (Fig. 4) [6].

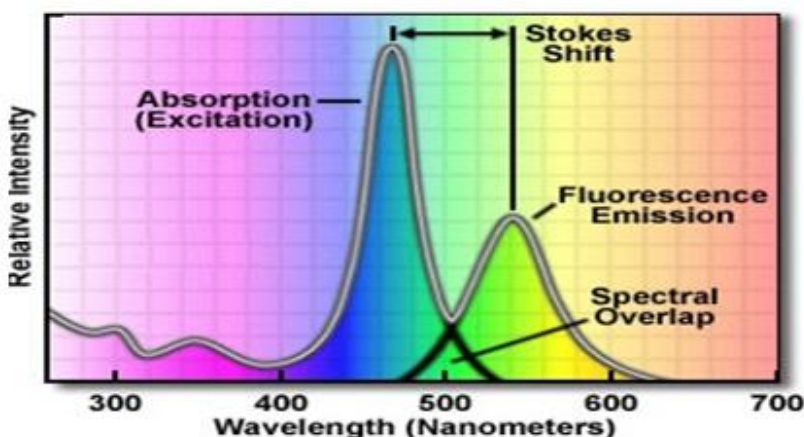


Figure 4: The emission spectrum is shifted to longer wavelengths than the excitation spectrum. This phenomenon is known as Stokes shift [49].

1.4.2 Tissue Absorption and absorption coefficient μ_a

Absorption phenomena are responsible for light attenuation in tissue. The interaction is dependent on the wavelength of the incident light and the type of the tissue[13]. Inside tissue, light can be absorbed by tissue absorbers, called *chromophores*. The probability of absorption is described by the *absorption coefficient* (μ_a) which is defined as the probability of absorption per unit length. The absorption coefficient depends on all the contributions to absorption by chromophores in the tissue. As a result of wavelength dependence, chromophores have different absorption spectra, as it is referred above. In Figure 5 is shown the absorption spectra of some important chromophores in human skin tissue.

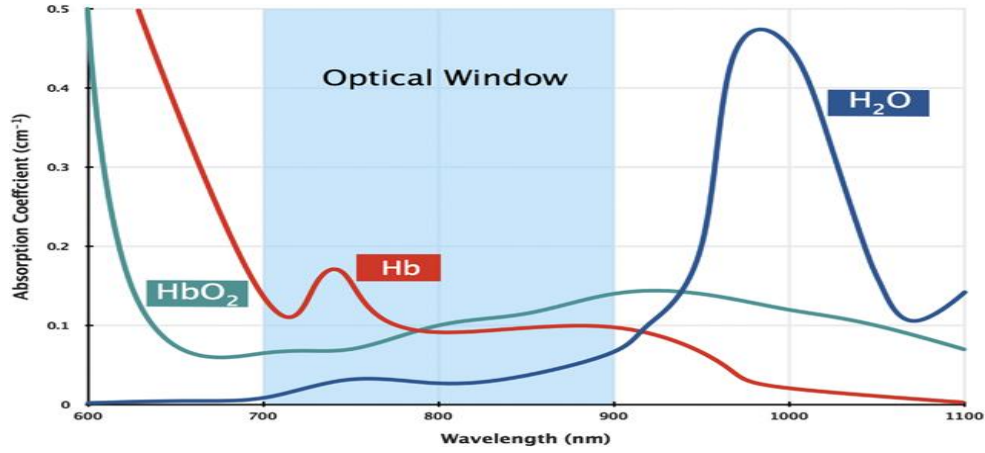


Figure 5: Absorption spectra of some important chromophores in human skin tissue, as function of wavelength [50].

Since the biggest part of the tissue is consisted of water, water is the most important absorber in tissue. Other important chromophores in tissue are haemoglobin and melanin. The absorption of light by blood depends on the oxygenated (HbO₂) and deoxygenated (Hb) haemoglobin (Fig. 5). The low-absorbing region between approximately 630 nm and 1300 nm is referred as the tissue optical window. In this range, the penetration of light into biological tissue is at its deepest [14]. For a single absorber, the *absorption cross section* σ_a , which indicates the absorbing capability, is related to its geometric cross-sectional area σ_g through the absorption efficiency Q_a .

$$\sigma_a = Q_a \sigma_g \quad (1)$$

In a media which contains many absorbers with *number density* N , the absorption coefficient can be considered as the total cross-sectional area for absorption per unit volume:

$$\mu_a = N\sigma_a (cm^{-1}) \quad (2)$$

1.4.3 Scattering in tissue and Scattering coefficient μ_s

When light passes through tissue it can be attenuated by scattering and by absorption as it is referred in the previous paragraph. Only part of the light will be transmitted. There are two major types of scattering events. If the frequency of the scattered wave is equal to that of the incident wave, it is called *elastic scattering*, but if the frequency of the incident wave and the scattered wave differs, it is called *inelastic scattering*. There are two important types of elastic scattering, *Rayleigh* and *Mie* scattering. Rayleigh scattering happens when the size of the scatterers (molecules and very tiny particles) are much smaller than the wavelength of the incident wave (up to about a tenth of the wavelength). Mie scattering predominates when the size of the scatterers are larger than the wavelength of the incident light. In a medium which contains many scatterers that are randomly dispersed in space, photons come over multiple scattering events. Scattering in tissue is due to several optical effects[15] a) reflection and refraction of light from interfaces between materials having different refractive indices, b) reflection of light by discrete particles in the tissue ranging from organic molecules to whole cells, c) absorption of light rays by atoms and molecules and re-radiation at the same wavelength but in other directions. In all these procedures the direction of light changes due to the scattering, and no energy loss is involved [16]. Scattering in turbid media is described by the *scattering coefficient* μ_s which is defined as the probability of scattering per unit length and describes the average of how many times per unit length a photon change its direction. For a single scatterer, the *scattering cross section* σ_s , which indicates the scattering capability, is related to its geometric cross-sectional area σ_g , through the scattering efficiency Q_s .

$$\sigma_s = Q_s\sigma_g \quad (3)$$

For a medium containing many scatterers with number density N , the scattering coefficient can be considered as the total cross-sectional area for scattering per unit volume:

$$\mu_s = N\sigma_s \text{ (cm}^{-1}\text{)} \quad (4)$$

The average distance a photon travels between scattering events, is called the mean free path length (MFP), and is defined as:

$$MFP_s = \frac{1}{\mu_s} \text{ (cm)} \quad (5)$$

In tissue, scattering is not isotropic, but forward directed [16, 17]. For complete description of scattering event we need to describe single scattering phase function. It is due to the spatially dependence of continuing photons. This function is denoted as $p(\hat{s}, \hat{s}')$, where direction of the incident photon is described by vector \hat{s} and direction of the scattered photon by \hat{s}' . Scattering depends only on the angle θ between unit vector directions \hat{s} and \hat{s}' (Fig. 6). The angular dependence of scattering, called the probability distribution function or scattering phase function. It is a function of the scattering angle such that[18]:

$$p(\hat{s}, \hat{s}') = p(\theta) \quad (6)$$

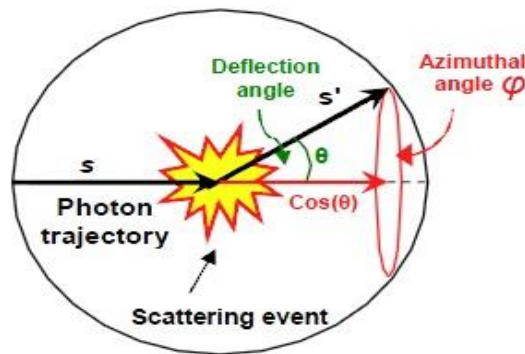


Figure 6: A scattering event causes a deflection at angle θ from the original direction \hat{s} to the direction \hat{s}'

Phase function can be represented by anisotropy factor g which describe the mean cosine of the scattering angle and it can be defined by [19]:

$$g = \int_{4\pi} p(\theta, \varphi) \cos(\theta) d\omega \quad (7)$$

The anisotropy factor g can have absolute values from 0 to 1, from isotropic scattering ($g = 0$) to forward scattering ($g = 1$). Negative values for g stand for backward scattering. For biological tissue the value of g is usually 0.9, which describes a mainly forward scatter for the tissue.

In case where the anisotropy of the medium is taken into account, then we have to describe *the reduced scattering coefficient* μ'_s , which can be defined as:

$$\mu'_s = \mu_s (1 - g)(cm^{-1}) \quad (8)$$

The purpose of μ'_s is to describe the diffusion of photons in a random walk of step size of $1/\mu'_s$, called reduced/transport mean free path length, where each step involves isotropic scattering [17]:

$$MFP'_s = \frac{1}{\mu'_s} (cm) \quad (9)$$

Such a description is equivalent to description of photon movement using many small steps $1/\mu'_s$ that each involves only a partial deflection angle θ . This way to describe light propagation becomes important in cases where there are many scattering events before an absorption event, i.e. $\mu_a \ll \mu'_s$ (fig. 7).

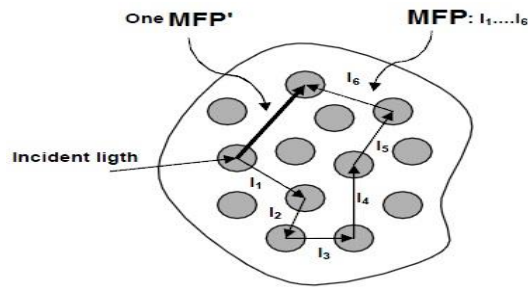


Figure 7: The equivalence of 6 small steps of $MFP = 1/\mu_s$ with one $MFP' = 1/\mu'_s$ [17].

1.4.4 Total Attenuation coefficient μ_t

According to the previous paragraphs, the photon can be absorbed or scattered. So, the total attenuation of the light is affected by both of these events. For a medium containing both scatterers and absorber with number density N , the total macroscopic cross-section (σ_t), the total attenuation coefficient μ_t is described as following:

$$\mu_t = N\sigma_t = N(\sigma_a + \sigma_s)(cm^{-1}) \quad (10)$$

2.1 Photon transport models based on Radiative Transfer Equation (RTE)

In order to describe the propagation of light, which means the photon transport into a media, a mathematical model should be used. Photon transport in biological tissue can be modeled analytically by the Radiative Transfer Equation (RTE) for visible or near-infrared light. Let suppose that $\Omega \subset \mathbb{R}^n$, $n=2$ or 3 denote the physical domain and $\partial\Omega$ the boundary of the domain, and let $\hat{s} \in S^{n-1}$ denote a unit vector in the direction of interest. If the accepted RTE model is used to describe the propagation in tissues, the frequency and the time domain version will be written as following:

$$\left(\frac{i\omega}{c} + \hat{s} \cdot \nabla + \mu_s + \mu_a\right) \varphi(r, \hat{s}) = \mu_s \int_{S^{n-1}} \varphi(r, \hat{s}') p(\hat{s} \cdot \hat{s}') d\hat{s}' + q(r, \hat{s}) \quad (11)$$

$$\left(\frac{1}{c} \frac{\partial}{\partial t} + \hat{s} \cdot \nabla + \mu_s + \mu_a\right) \varphi(r, \hat{s}) = \mu_s \int_{S^{n-1}} \varphi(r, \hat{s}') p(\hat{s} \cdot \hat{s}') d\hat{s}' + q(r, \hat{s}) \quad (12)$$

Where i is the imaginary unit, ω is the angular modulation frequency of the input signal, c is the speed of light in the medium, μ_s and μ_a are the scattering and absorption coefficients of the medium, respectively, $\varphi(r, \hat{s})$ is the radiance, and $q(r, \hat{s})$ is the source inside Ω [21]. The kernel $p(\hat{s} \cdot \hat{s}')$ is the scattering phase function which describes the probability that a photon with an initial direction \hat{s} will have a direction \hat{s}' after a scattering event. Two important measurable parameters that derived from the above, which are of interest are [21]:

Photon density

$$\Phi(r, t) = \int_{S^{n-1}} \varphi(r, \hat{s}, t) d\hat{s} \quad (13)$$

Photon current

$$J(r, t) = \int_{S^{n-1}} \hat{s} \varphi(r, \hat{s}, t) d\hat{s} \quad (14)$$

Since the RTE is a complicated model to be solved, there are some approximations to it. One of these approximations is the Diffusion Approximation (DA) that provides solutions that are more computationally efficient but accurate under some conditions [6],[20]. If we suppose that the anisotropy factor $g=1$ [21]:

Isotropic source:

$$q_0 = q_{0,0} \quad (15)$$

Transport coefficient:

$$\mu_t = \mu_s + \mu_a \quad (16)$$

Reduced scattering coefficients:

$$\mu'_s = (1 - g)\mu_s \quad (17)$$

Diffusion coefficient:

$$D = \frac{1}{3(\mu_a + \mu'_s)} \quad (18)$$

Then from the equations Eq.11 and Eq.12 we can obtain the more known form of the above quantities:

$$\left(\frac{1}{c} \frac{\partial}{\partial t} + \mu_a(r) \right) \Phi(r, t) + \nabla \cdot J(r, t) = q_0(r, t) \quad (19)$$

And

$$\left(\frac{1}{c} \frac{\partial}{\partial t} + \frac{1}{3D(r)} \right) J(r, t) + \frac{1}{3} \nabla \cdot \Phi(r, t) = q_1 \quad (20)$$

2.1.1 Diffusion Theory and its approximation for Optical/Fluorescence Imaging

The diffusion approximation results from making the assumptions that [21]:

$$\frac{\partial J}{\partial t} = 0 \text{ and } q_1 = 0 \quad (21)$$

As a result of that it gives:

$$-\nabla \cdot D(r) \nabla \Phi(r, t) + \mu_a \Phi(r, t) + \frac{1}{c} \frac{\partial \Phi(r, t)}{\partial t} = q_0(r, t) \quad (22)$$

With frequency domain:

$$-\nabla \cdot D(r) \nabla \Phi(r, \omega) + \mu_a \Phi(r, \omega) + \frac{i\omega}{c} \Phi(r, \omega) = q_0(r, \omega) \quad (23)$$

$\Phi(r)$ is the photon density, and $q_0(r)$ is the source inside the domain Ω . Important condition for the diffusion approximation to be valid is that $\mu_a \ll \mu_s$ [21].

2.1.2 Boundary Conditions and Source Terms

To use the diffusion approximation (DA) for our problems we need to impose certain boundary conditions that no photons travel in an inward direction at the boundary, except at the sources [21]. If the mismatch between the refractive indices of the medium and surrounding medium is taken into account, a Robin type boundary condition can be derived [22] and it has the form:

$$\Phi(r) + 2\zeta D \frac{\partial \Phi(r)}{\partial \vec{n}} = 0, \quad r \in \partial\Omega \quad (24)$$

Where ζ is a boundary term incorporating the refractive index mismatch at the surface of the medium. The light source is modeled as an isotropic point source located at a depth $1/\mu'_s$ below the source site. A collimated source incident at $p \in \partial\Omega$ commonly is represented by a diffuse point source as following [21], [23]:

$$q_0(r) = \delta(r - r_s) \quad (25)$$

Where r_s is set at depth $1/\mu'_s$. This has as a result that the exponentially line source, where the photons are travelling in a direction $-\tilde{n}$, in respect to the distance z has probability [21]:

$$P(z) = e^{-\mu_\tau z} \quad (26)$$

There are some analytic solutions for the exponentially decaying line source. They include the spatial distribution over the surface and a finite element model (FEM) is involved. This method investigates several source models, making the specification that the source has the Dirichlet or Neumann boundary condition [25],[26].

2.2 Overview of the Tomographic Imaging Reconstruction Problem

In the FMT system, light in an excitation wavelength coming from an appropriate laser source is shined on the surface of the biological sample under investigation in a transmission or reflection setup fig22. A CCD camera looking at the sample is acquiring two sets of measurements in the Excitation and Fluorescence wavelengths using appropriate filters. Thus, measurements are obtained in the form of images which in turn contain information about the transmission of excitation light to the fluorescence sources and the re-emission of fluorescence light from the fluorophore targets to the surface of the sample. So these measurements contain information about the physical attributes of the sample. To achieve the reconstructed distribution map of a certain physical attribute (e.g. absorption, scattering, fluorescence, etc) a model that mathematically describes how the measurements are related to the physical attributes that we want to determine is necessary. Such a model enables the calculation of synthetic data corresponding to the actual measurements, for a known set of physical attributes, through the so-called forward mapping. Determining the physical attributes then involves the inversion of the forward model, in other words inverse mapping of actual measurements, so that simulated measurements match, as close as possible, the actual measurements. The mathematical framework of the reconstruction in FMT for this project is given by the combination of a forward model for light propagation and an inverse model for reconstructing distribution of fluorescence targets [23] , and it is described in further detail in the following paragraphs.

2.2.1 The Forward Model

The aim of the forward modeling in our case is to model the transportation of light through the biological tissue, to do so we solve the diffusion equation, with known optical properties for a specific sample geometry. The method has extensively been used in diffusion optical tomography (DOT) [6],[25] describing the propagation of near-infrared light (NIR) through biological tissues. We use an appropriate continuous wave (CW) source located at r_s and detectors in the position r_d . The source illuminates the surface of our sample and the detector(s) collect the average light intensity which is recorded on the surface. In order to have an accurate model to describe the propagation parameters such as the shape/geometry of the sample, the optical properties of the sample (μ_a , μ_s , n) and the location of the sources and detectors need to be known. Here in this work, to solve the diffusion equation in realistic geometries the finite element model (FEM) is used [24], [25], [26].

2.2.2 Computational method - The finite element method (FEM)

In the FEM procedure, the domain Ω is divided into P elements. These elements are joined at D vertex nodes. The solution of Φ is approximated by the piecewise function[21]:

$$\Phi^h(r, t) = \sum_i^D \Phi_i(t) u_i(r) \in \mathcal{U}^h \quad (27)$$

Where \mathcal{U}^h is a finite-dimensional subspace spanned by basis functions $u_i(r)$ ($i = 1 \dots D$). The solution for Φ^h is one of sparse matrix inversion. The advantage of using FEM is its flexibility which makes it practicable to complex geometries and highly inhomogeneous parameter distributions [21].

2.2.3 The Inverse Model

One of the biggest problems in Optical Imaging is to recover the optical properties of the tissues from boundary measurements. The image reconstruction in DOT is an ill-posed nonlinear

inverse problem. The key tool, to achieve the reconstruction, is to study the inverse problem by using the linearization of the forward map p which is the problem of finding the fluorescence source distribution from measured light intensities on the tissue surface. In order to overcome the ill-posedness a very promising procedure for the solution of the inverse problem is to use prior information such as anatomical shape of our sample, for example the shape of the mouse. This has been successfully used for the case of the Diffuse Optical Tomography (DOT) where the reconstruction is mainly for the optical properties[25],[26]. The anatomical information can be used into the forward and/or inverse problem formulations of the FMT model. As referred above the imaging is an indirect method. Image x has to be inferred from data y through the inversion of using the forward model [21]. In our case, the image reconstruction is an implicit method. It can be considered a non-linear optimization approach. The forward model for the light transport can estimate the readings from the detectors on the tissue boundary for a given initial source distribution. An objective function ψ is defined in order to compare the predicted and measured detector's readings. Then, the optimization process is finished after the minimum of the objective function is found and the measured and predicted data match.

The key tool for the study of the inverse problem is the linearization of the forward map p . In other words we have to achieve the following scheme [21]:

Forward problem:

Given sources $\{q\}$ and $(a,b) \in X^{(a)}(\Omega), X^{(b)}(\Omega)$. Find the data $\{y\} \in \partial\Omega$.

Inverse problem:

Given sources $\{q\}$ and data $\{y\} \in \partial\Omega$. Find the $(a,b) \in X^{(a)}(\Omega), X^{(b)}(\Omega)$.

The forward problem can be represented non-linearly as:

$$y = p(a, b) \tag{28}$$

In this form (a,b) are the absorption and scattering coefficient, respectively. The parameters in this scheme to deal with are:

- S (the number of the sources), source position j ($j=1\dots S$),
- M_j measurements positions for the source j , $M_{tot} = \sum_{j=1}^S M_j$
- the absorption coefficients μ_a and scattering coefficients μ_s

One common scheme to solve the inverse problem is to use the Jacobian matrix, which depends on the number of measured data and of the geometry used for the numerical solution. The Jacobian defines the derivative of the forward operator with respect to given parameter distributions. It is an important element of many reconstruction algorithms[27], [28], [29]. In this point there is the adjoint problem which can be solved either by explicitly constructing the Jacobian and Hessian matrices of the forward operator, or by an implicit, matrix-free approach [29].

2.3 Imaging Package tools for DOT in Matlab.

To simulate the light propagation in highly scattering media with complex boundaries, for example the brain of a mouse, we decided to use the solution to the diffusion equation on complex geometries. A tool that is commonly used for its numerical solution is the Finite Element Method (FEM). Instead of creating our own solution to the diffusion using FEM we decided to use the software environment **Toast++** that has been developed in order to solve the forward and inverse problems in Diffuse Optical Tomography (DOT) and in its current version stands as a *Matlab toolbox* and its open source includes tools that can model steady-state, time and frequency domain data acquisition systems. It is built on a FEM based forward solver and it contains model-based iterative inverse solvers for the reconstruction of the 3D distribution of absorption and scattering parameters from boundary measurements of light transmission. Toast++ also provides a range of regularization methods, taking into account the incorporation of the prior knowledge of internal structure [30]. To use the finite element solver, there is a need to create *the mesh* of our sample. A mesh is presented by a list of elements and an associated list of nodes. There exists a variety of mesh generation software that someone can use to create a mesh from initial medical imaging voxel-based volumetric images, either commercial or research based, like the *iso2mesh* toolbox. It is a free matlab/octave-based mesh generation and processing toolbox. It can create 3D tetrahedral finite element (FE) mesh from surfaces, 3D binary and gray-scale volumetric images.

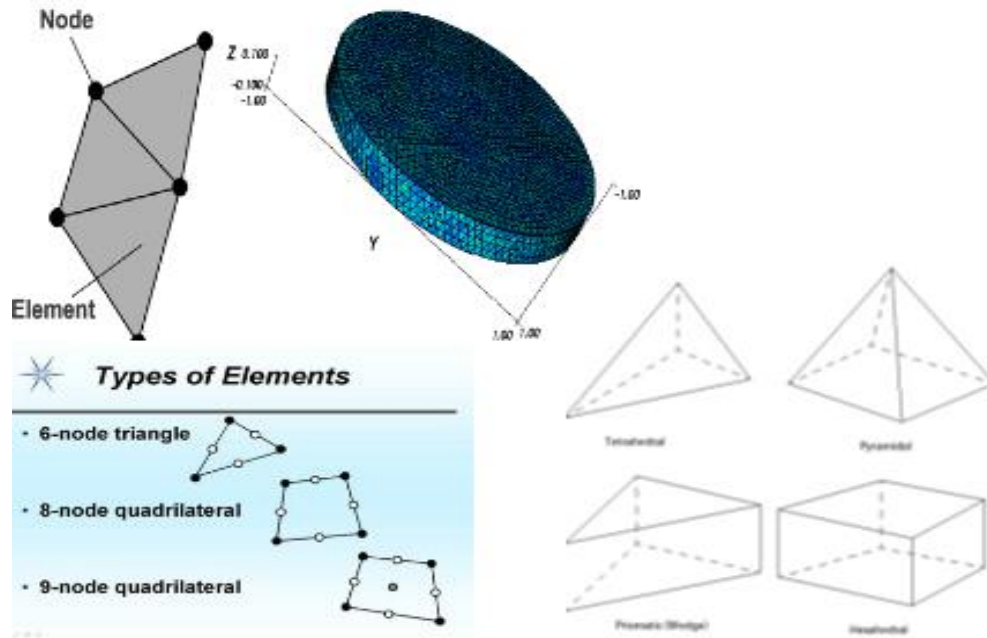


Figure 8: Nodes and elements (left up) and how a mesh looks like (right up), 2D types of elements and 3D types of elements.

A mesh also holds data about the absorption and scattering parameters associated with each element and this can be included to the FEM solvers procedure. Also there are developed routines that generate meshes from images[30], [31] as it is shown below (Fig 9).



Figure 9: Low resolution FEM gray scale mesh human head constructed from 2D MRI scan. The color indicates absorption coefficient [30].

A general characteristic of the meshes is the number of elements and nodes they will use to approximate a certain geometry. The larger the number of elements/nodes is, the better the approximation of the geometry and the solution of the numerical method will be, but at the same time this translates to large system matrixes and therefore harder computational effort. Mesh optimization methods can be employed to optimize the size of a mesh for each application and geometry. The node list of a mesh is an ordered sequence where each node has an associated number defined by its position in the list. The node number corresponds to the row and the column numbers for this node in an FEM system matrix.

3.1 Introduction in 3D Scanning Technology

Laser scanning is the process of recording precise three dimensional information of a real world object or environment. Laser scanners rapidly sample or scan an object's surface recording shape and often visual properties (intensity and/or RGB information). The information is returned as a dense collection of precisely measured XYZ points referred to as a point cloud.

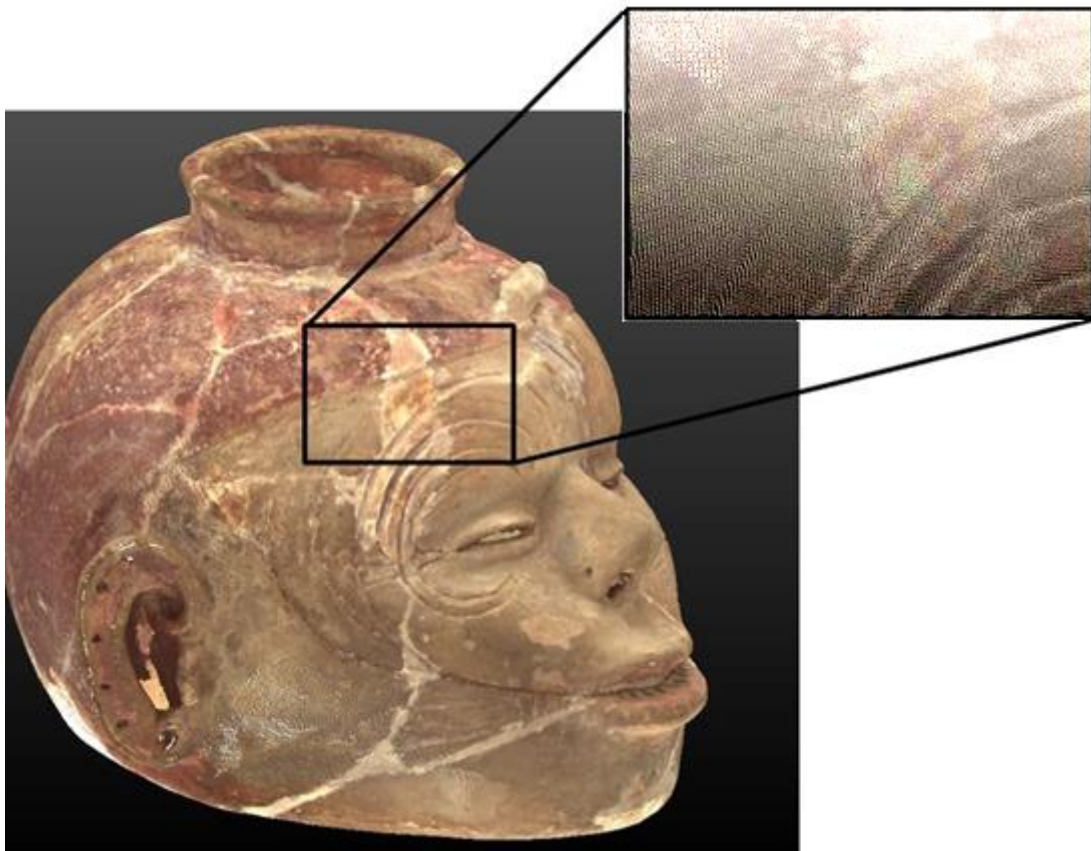


Figure 10: Point cloud example [51].

Point clouds produced by laser scanners contain a wealth of information on their own and can also be processed to create accurate 3D models of objects and environments as well as a host of other derivatives that are useful in a wide range of applications. There are different principles used in the 3D scanning technology, but in this work we are dealing with scanners based on the triangulation method [44].

3.2 The basic principles of laser triangulation

Laser triangulation is based on the projection of a laser over an object and the image is captured by a camera. The 3D position of the laser beam over the object can be calculated by trigonometry, if we know the distance between the laser source and the camera (called baseline) and the angle between the baseline and the laser beam [44]. An example of the triangulation system configuration is shown in Figure 11 and Figure 12.

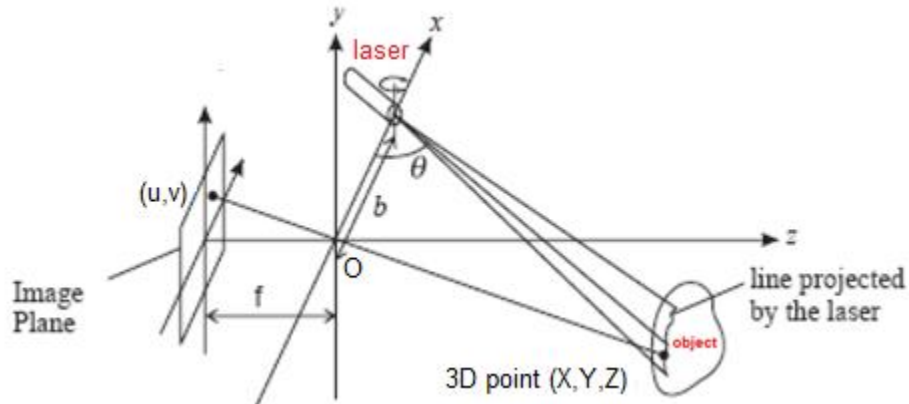


Figure 11: Example of triangulation system. The coordinate (X, Y, Z) of a 3D point in real space which is projected onto the image pixel (u, v) [44].

In order to find the parameters of the camera, a calibration procedure should be done. The procedure of calibration has an important role in the scanning process and affects the scanner's precision.



Figure 12: Laser triangulation: 3D scene and 2D camera image [52].

3.3 Camera Calibration

There are many techniques used to calibrate the camera [44] but in our case we use 2D plane-based calibration which requires observation of a planar pattern shown at few different orientations [44]. The camera follows the pinhole model in which a scene view is formed by projecting 3D points into the image plane using a perspective transformation.

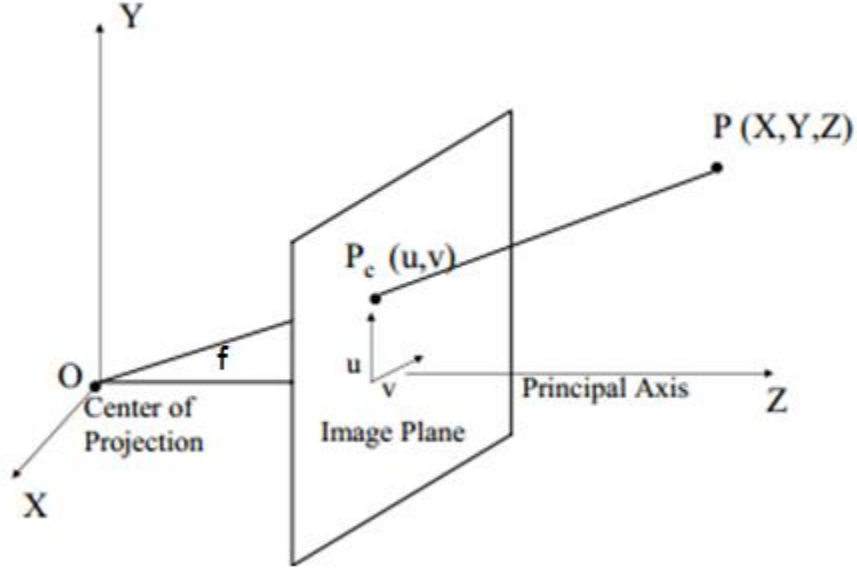


Figure 13: The pinhole camera model [45].

The Figure 13 shows a camera with center of projection O and the principal axis parallel to Z axis. Image plane is at focus and hence focal length f away from O. A 3D point $P = (X, Y, Z)$ is imaged on the camera's image plane at coordinate $P_c = (u, v)$. We will first find the camera calibration matrix C (or projective matrix) which maps 3D points (P) to 2D image (P_c). We can find P_c using similar triangles as [44], [45]:

$$\frac{f}{Z} = \frac{u}{X} = \frac{v}{Y} \quad (29)$$

$$u = \frac{f X}{Y} \quad (30)$$

$$v = \frac{fY}{Z} \quad (31)$$

Using homogenous coordiantes for P_c we can write this as:

$$\begin{pmatrix} u \\ v \\ w \end{pmatrix} = \begin{pmatrix} f & 0 & 0 \\ 0 & f & 0 \\ 0 & 0 & 1 \end{pmatrix} \begin{pmatrix} X \\ Y \\ Z \end{pmatrix} \quad (32)$$

Next, if the origin of the 2D image coordinate system does not coincide with where the Z axis intercests the image plane, we need to translate P_c to the desired origin. Let this translation be defined by (t_u, t_v) . Hence (u, v) is defined by [44],[45]:

$$u = \frac{fX}{Y} + t_u \quad (33)$$

$$v = \frac{fY}{Z} + t_v \quad (34)$$

$$\begin{pmatrix} u \\ v \\ w \end{pmatrix} = \begin{pmatrix} f & 0 & t_u \\ 0 & f & t_v \\ 0 & 0 & 1 \end{pmatrix} \begin{pmatrix} X \\ Y \\ Z \end{pmatrix} \quad (35)$$

P_c is expressed in pixel/inches, since this is a camera image. Due to this we will need to know the resolution of the camera in pixels/inch. If the pixels are square the resolution will be identical in both u and v directions of the camera image coordinates. However, for a more general case, we assume rectangle pixels with resolution m_u and m_v pixels/inch in u and v direction respectively. Therefore, to measure P_c in pixels, its u and v coordinates should be multiplied by m_u and m_v respectively. This can be expressed in matrix form as[44],[45]:

$$\begin{pmatrix} u \\ v \\ w \end{pmatrix} = \begin{pmatrix} m_u f & 0 & m_u t_u \\ 0 & m_v f & m_v t_v \\ 0 & 0 & 1 \end{pmatrix} \begin{pmatrix} X \\ Y \\ Z \end{pmatrix} = \begin{pmatrix} a_x & 0 & u_o \\ 0 & a_y & v_o \\ 0 & 0 & 1 \end{pmatrix} P = KP \quad (36)$$

The matrix K only depends on the intrinsic camera parameters like its focal length, principal axis and thus defines the intrinsic parameters of the camera. Sometimes K also has a skew parameter s , given by:

$$K = \begin{pmatrix} a_x & s & u_0 \\ 0 & a_y & v_0 \\ 0 & 0 & 1 \end{pmatrix} \quad (37)$$

This usually comes in if the image coordinates axes u and v are not orthogonal to each other. Note that K is an upper triangular $[3 \times 3]$ matrix. This is usually called the *intrinsic parameter matrix* for the camera. If the camera does not have its center of projection at $(0, 0, 0)$ and is oriented in an arbitrary fashion (not necessarily z perpendicular to the image plane), then we need a rotation and translations to make the camera coordinate system coincide with the configuration of the pinhole model. Let the camera translation to origin of the (XYZ) coordinate be given by $T(T_x, T_y, T_z)$. Let the rotation applied to coincide the principal axis with Z axis be given by a $[3 \times 3]$ rotation matrix R . Then the matrix formed by first applying the translation followed by the rotation is given by the 3×4 matrix:

$$E = (R|RT) \quad (38)$$

called the *extrinsic parameter matrix*. So, the complete camera transformation can now represented as:

$$K(R|RT) = (KR|KRT) \quad (39)$$

Hence P_c , the projection of P is given by:

$$P_c = (KR|KRT)P = CP \quad (40)$$

C is a 3×4 matrix usually called the complete camera calibration matrix or projective matrix. Thus, given C , we can find the intrinsic and extrinsic parameters through this process. To find C for any general camera, we need to find *correspondences* between 3D points and their projections on the camera image. If we know a 3D point P corresponding to P_c on the camera image coordinate, then $P_c = CP$. Note that finding C means we have find all the 12 entries of C . To solve for 12 unknowns, we will need at least 6 such correspondences. Usually for better accuracy, much more than 6 correspondences are used and the over-determined system of

linear equations thus formed is solved using singular value decomposition methods to generate the 12 entries of C . The correspondences are determined using fiducial based image processing methods [44],[45].

Because the camera has not a perfect geometry there are some distortion concerning the position of image points in the image plane. As a result of several types of imperfections in the design and assembly of lenses composing the camera optical system there are some positional errors (or distortion). There are three types of distortions. The first one is caused by imperfect lens shape and manifests itself by radial positional error only, whereas the second and the third types of distortion are generally caused by improper lens and camera assembly and generate both radial and tangential errors in point positions (see Fig).

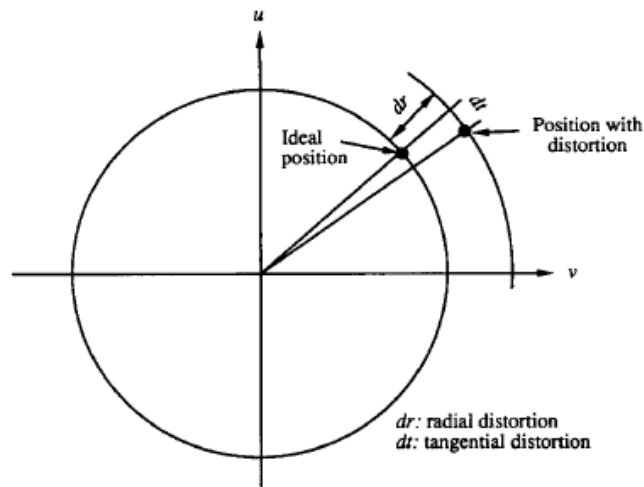


Figure 14: Radial and tangential distortion [45].

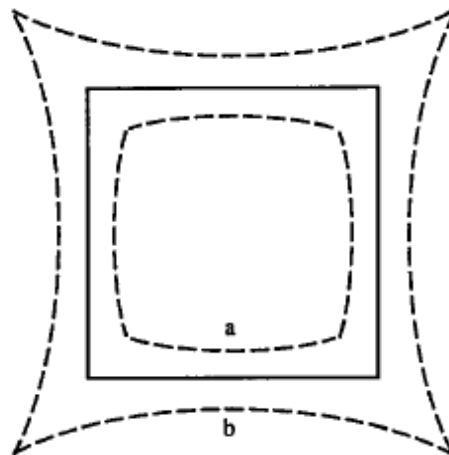


Figure 15: Effect of radial distortion. Solid lines: no distortion; dashed lines: with radial distortion (a: negative, b: positive) [45].

Part B. Experiments and Results

Material, Phantoms, Tools and Methods

For the achievement of the project various tools and methods are used and their description and methodology followed will be presented. As it is referred above the concept of this work is to optimize the Fluorescence Molecular Tomography (FMT) imaging by adding prior information to the inversion procedure. In the framework of this dissertation this consist of the recovery of the absorption and scattering distributions over the domain of the mouse and the development of a 3D scanning device for acquiring the shape of the mouse's boundary surface of the mouse. The scheme of the methodology is described below (fig. 17):

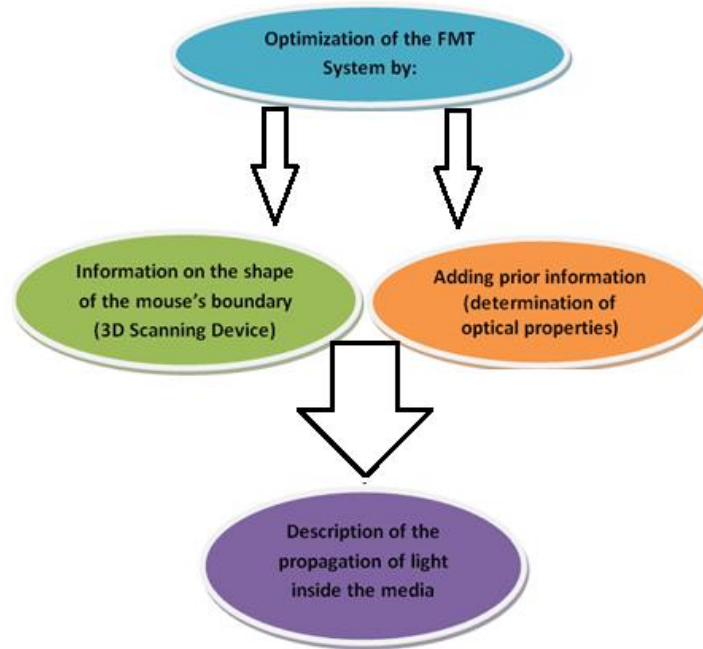


Figure 16: The scheme of the methodology.

Each part of the project is analyzed separately in order to be combined in one procedure which is essential for the optimization of our system. In each area different tools and materials are used.

4.1 Determination of the Optical Properties of phantom's materials

As we see above optical properties have an important role in optical imaging. There are many models that are used for the determination of the optical properties[32],[33].

Here we will use a photometric method for the determination of optical properties (μ_a, μ'_s) for materials that will be used for the creation of optical phantoms. One of the popular and easy-to-use calculation models, using parameters measured from a spectrophotometer, is the two-flux Kubelka–Munk model. It uses measurements of transmission and reflection for a sample to calculate absorption and scattering. This method is valid under conditions of strong light scattering, when the thickness of the specimen considerably exceeds transport length[32],[33]:

$$MFP'_s = \frac{1}{(\mu_a + \mu'_s)} \quad (41)$$

According to the Kubelka–Munk model, the relation between the measured Transmission and Reflection to the Absorption and scattering is as follows[33]:

$$A_{KM} = 2\mu_a, \quad S_{KM} = \frac{3\mu'_s}{4} - \frac{\mu_a}{4} \quad (42)$$

For a flat layer with thickness d , the characteristics of the medium are obtained through the measured diffuse transmittance and reflectance as below [33]:

$$S_{KM} = \frac{1}{d\sqrt{a^2 - 1}} \ln \left[\frac{1 - R_d(a - \sqrt{a^2 - 1})}{T_d} \right] \quad (43)$$

Where:

$$A_{KM} = S_{KM}(a - 1), \quad a = \frac{(1 + T_d^2 + R_d^2)}{2R_d} \quad (44)$$

The limit of this model is in media that strongly absorb light and relatively weakly scatter ($\mu'_s < \mu_a/3$).

In this part of the project phantoms are used to represent the tissue of the mouse. Most of the phantoms available in literature or in the market have simple geometrical shapes (cubes, slabs, cylinders). If they have a realistic shape they usually have homogeneous approximations to the optical properties of the tissue of the animal under investigation. In our case, we use specimens in order to reach a multilayer phantom [38] as it is shown in the figure 18. The final shape of the phantom has the structure shown in fig 17.

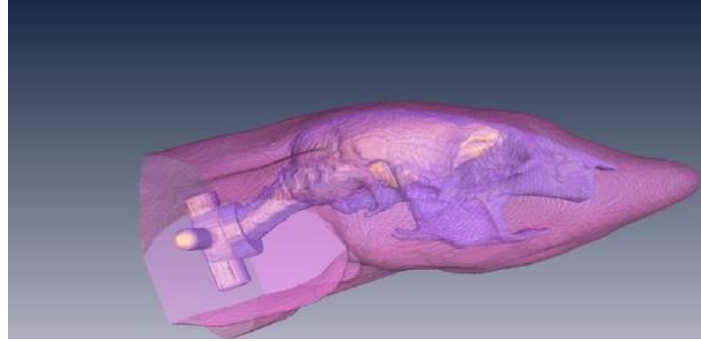


Figure 17: The final three layer digital prototype of the mouse head phantom [38].

The study for each type of tissue has to be done before the construction of the final multilayered realistic phantom. To do that we are going to assess the optical characteristics of the materials that will be used for the final phantom. To measure the optical properties and in order to minimize the parameters involved, we are going to use simple shaped specimens, more specifically homogeneous cylinders. To estimate their optical properties we are going to use a simple inversion based on the Diffusive Equation that describes how light propagate through the media.

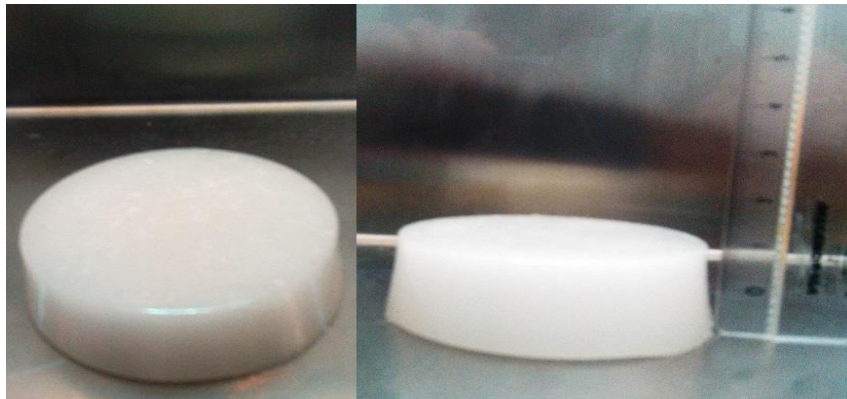


Figure 18: Specimens design.

Tissue ID	Tissue Type	MA (mm ⁻¹)	MS (mm ⁻¹)	Anisotropy (g)	Refract. Index (n)	Notes
1	skin	0.0191	6.6	0.9	1.37	skin here is actually soft tissue, use scalp data @830nm from Strangman2003
2	skeleton	0.0136	8.6	0.9	1.37	use skull from Strangman2003
3	eye	0.0026	0.01	0.9	1.37	use CSF from Strangman2003
4	medulla	0.0186	11.1	0.9	1.37	use brain from Strangman2003
5	cerebellum	0.0186	11.1	0.9	1.37	brain
6	olfactory bulbs	0.0186	11.1	0.9	1.37	brain
7	external cerebrum	0.0186	11.1	0.9	1.37	brain
8	striatum	0.0186	11.1	0.9	1.37	brain
9	heart	0.0240	8.9	0.9	1.37	muscle
10	rest of the brain	0.0026	0.01	0.9	1.37	use CSF from Strangman2003
11	masseter muscles	0.0240	8.9	0.9	1.37	muscle
12	lacrimal glands	0.0240	8.9	0.9	1.37	muscle
13	bladder	0.0240	8.9	0.9	1.37	muscle
14	testis	0.0240	8.9	0.9	1.37	muscle
15	stomach	0.0240	8.9	0.9	1.37	muscle
16	spleen	0.072	5.6	0.9	1.37	use rat liver data from Cheong1990
17	pancreas	0.072	5.6	0.9	1.37	use rat liver data from Cheong1990
18	liver	0.072	5.6	0.9	1.37	from Cheong1990
19	kidneys	0.050	5.4	0.9	1.37	use cow kidney @789nm from Cheong1990
20	adrenal glands	0.024	8.9	0.9	1.37	muscle
21	lungs	0.076	10.9	0.9	1.37	use pig lung @850nm from Cheong1990, change g to 0.9

Table 2: The optical properties of different tissue types. (http://mcx.sourceforge.net/cgi-bin/index.cgi?MMC/DigimouseMesh#Tissue_optical_properties)

The values of the optical parameters are obtained from DIGIMOUSE atlas (Fig. 19) [39]. To estimate the values of optical properties in phantoms, the specimens with different concentrations of pigment were measured in a spectrophotometer equipped with an integrating sphere system (Fig.12) [40]. The measurements obtained from the spectrophotometer are the diffuse reflectance and the diffuse transmittance. Using these parameters, the optical properties, absorption and scattering were calculated by fitting the commonly used Kubelka-Munk model that is referred in previous paragraphs.

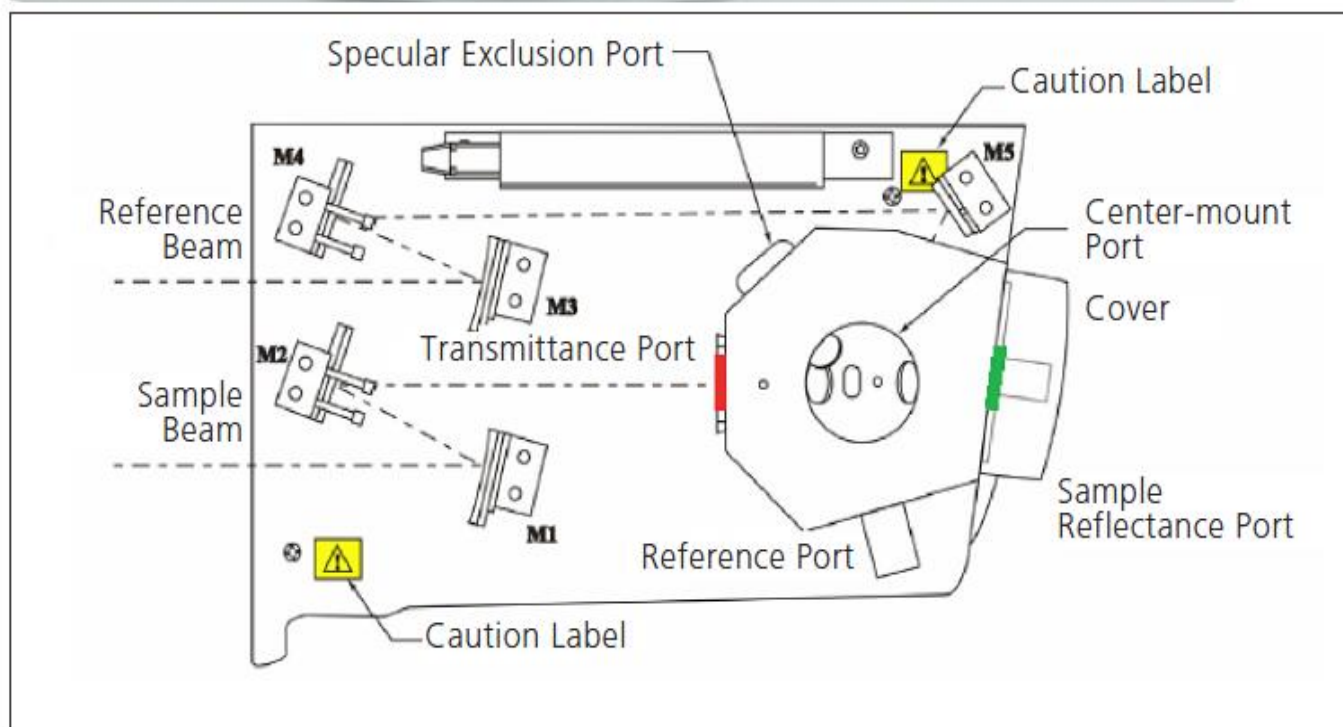


Figure 19: Picture of the 150 mm integrating sphere installed in the spectrophotometer PerkinElmer Lambda 950 with a top down view of the diagram of the sphere below. The red marked area is where Transmission of the material is done, and the green area the Reflectance of the material [40].

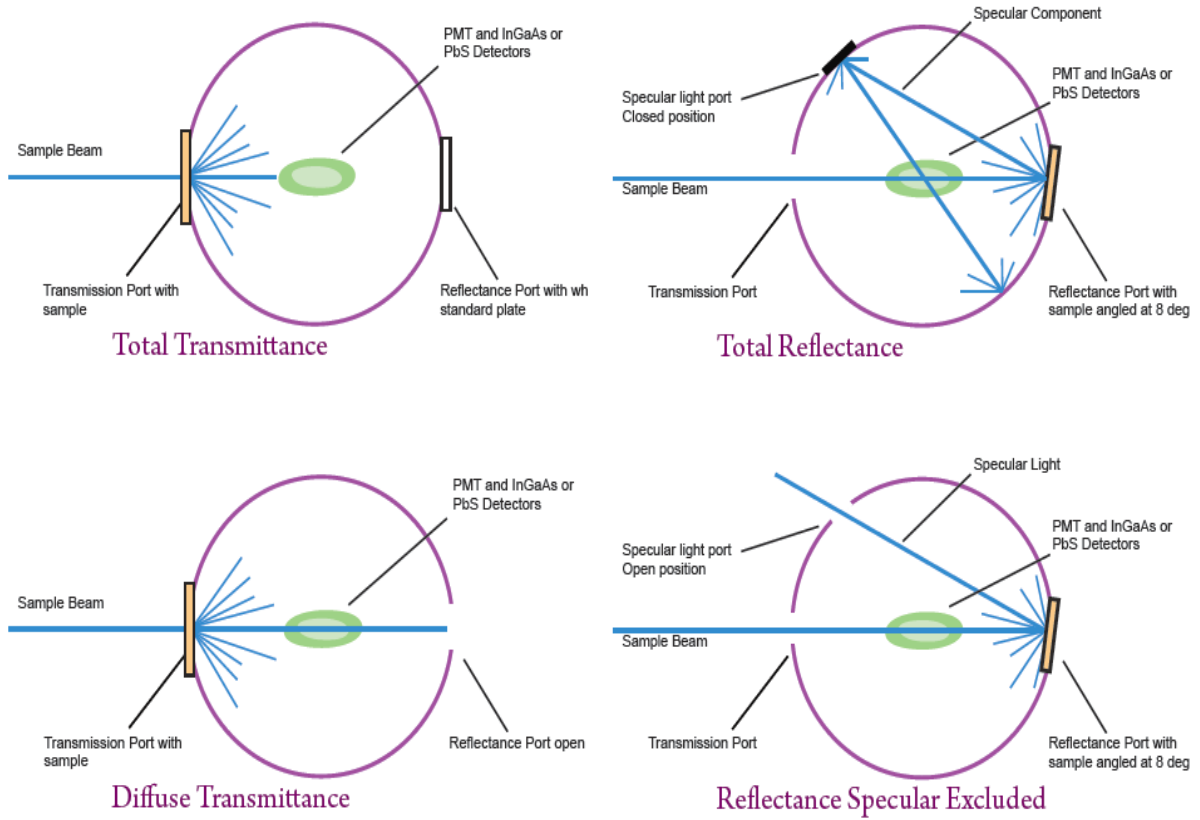


Figure 20: Spectrophotometer using integrating sphere measurements.

4.2 Description of the propagation of light inside the media and experimental procedure in FMT system.

To simulate all the procedure properly for the forward problem, the details of the experimental process should be included. The experimental data that are obtained in the FMT system follow the below schematic diagram.

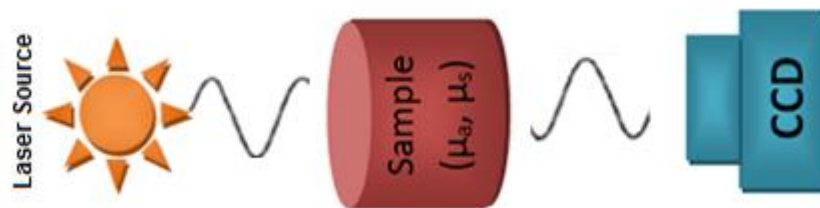


Figure 21: Representation of the experimental process.

The set-up of FMT system is consisted of three fundamental components: the laser sources, the sample and the detector (CCD). The source is a laser beam which is transmitted inside our sample.

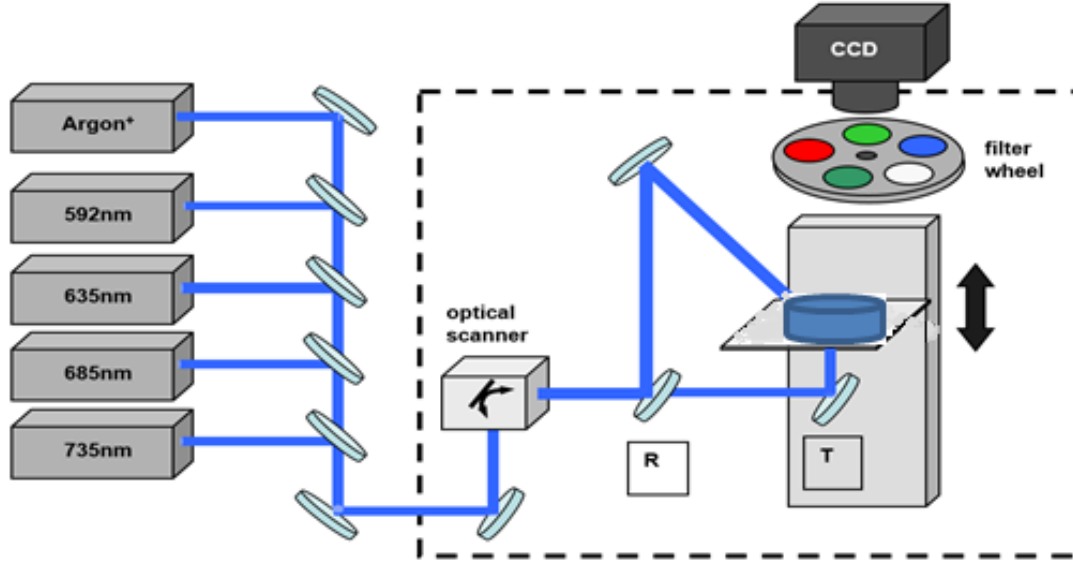


Figure 22: FMT set-up.

After the penetration the light is detected in the detector plane. This is the experimental measurement which will be used in the comparison with simulated data. To simulate the propagation of light through this media we are using the forward model which solves the DE using FEM. To simulate the experimental measurements the forward model includes inputs such initial guess of the optical properties of the media (μ_a, μ'_s), the location of the sources and detectors and the geometry of our sample in mesh representation. Solving the forward problem we have the simulated data (synthetic data). Once we have those two kinds of data (experimental and simulated) we can solve a simple inverse problem to check in what values of optical properties that we used for the simulation our data match with the experimental data. We set an objective function which presents the comparison of these two groups of data. We aspect in the minimum value of the objective function we have the match in the optical properties of the media.

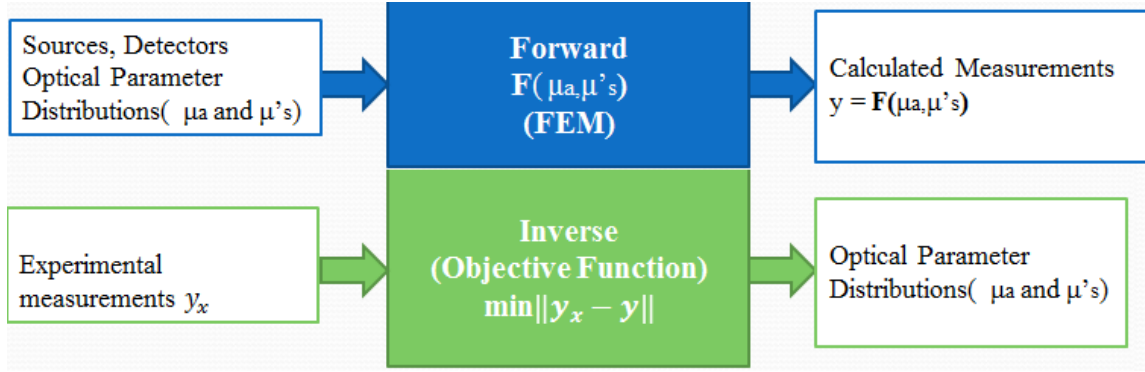


Figure 24: Schematic representation of the reconstruction (Forward and Inverse Model). The inversion works by comparing the real data obtained by FMT measurements (y_x) and the simulated data (y) for each guess of optical properties.

4.3 Information on the shape of the sample's boundary (3D scanning Procedure)

To solve properly the forward problem it is important to determine as many as possible of the parameters in the procedure. Giving information about the shape of the boundary of the object to be examined is one of the very important parameters taking place in the process. In this point we demonstrate an inexpensive 3D scanner procedure which is used in order to acquire the 3D shape of the mouse. The set-up is consisted by a web-camera, line-plane laser beam (scanning beam), two black planes placed in 90° angle, with known fiducials in the each surface of the plane, and a checkerboard, which is used to calibrate all the system. Due to the fact that the all set-up will be adjust in the FMT system, they colour of the planes should be black, for not affecting the experimental measuring procedure. The laser plane beam is used to scan the object, then the camera capture this real-time motions of the scanning in picture sequences. This scanning procedure is strongly affected by the reflectance of the surface of the object. Using the theory of Perspective Projection, the Pinhole model of the camera and one of the provided Camera Calibration toolbox it is possible to recover the 3D shape of an object in a 3D point clouds shape representation. The reconstruction part of the procedure is done by using triangulation, which is a common method for projected illumination patterns to contain identifiable lines or points in the scene, estimating that way the depth. After extracting and aligning the 3D point clouds shape it is possible to transform it into mesh volume using the appropriate algorithm but this goes further from this project and it will be done in future work

[34]. To understand and use the position of the camera in the 3D environment there is a need for an initialization in terms of calibration of the camera. Various techniques exist to calibrate the camera in order to recover the internal parameters of the camera through the imaging process. These parameters incorporate the focal length, the principal point and pixel skew. The classical calibration technique involves placing a calibration grid in the scene, for example a checkerboard, for which the coordinates of the intersections on the grid are known. The relationship between the coordinates of the intersections on the grid (markers) and the corresponding camera image coordinates of the same markers are the necessary input for the camera calibration.

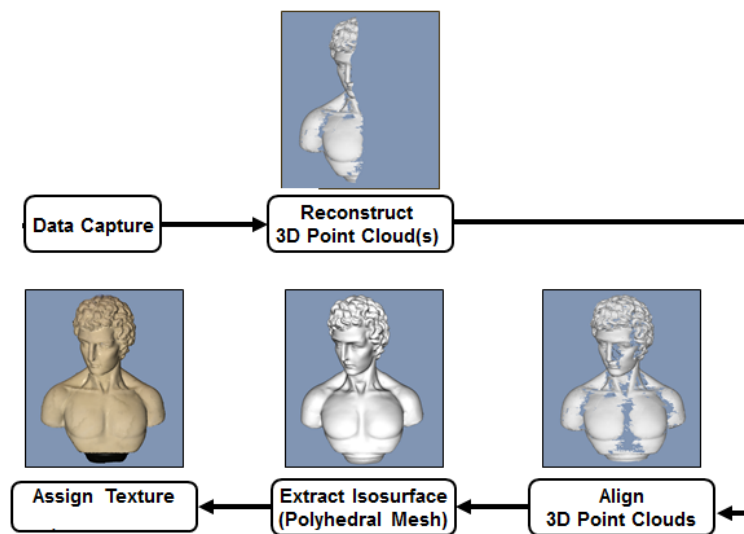


Figure 25: The procedure of optical Triangulation [34].

The laser plane beam is used to scan the surface of the object. The deflection of the laser plane defines a 3D plane. The depth is recovered by the intersection of this plane with the set of lines passing through the 3D ray on the surface. Using a geometric relation the depth at each pixel can then be recovered [34]. The parts of this procedure involve the following main functions [34]:

- Manually-assisted intrinsic camera calibration
- Manually-assisted extrinsic camera calibration
- 3D scanning with laser line planes
- Video capture using Image Acquisition Toolbox

We define four fiducials on each board the four corners of a rectangle with known side lengths. For the scanning we use a modified laser pointer with cylindrical lens fixed in front to create plane shaped beam. Once the setup is constructed initialization of the camera position should be performed using a calibration procedure to estimate the intrinsic calibration parameters of the camera using image sequences [36],[37]. Once the calibration has been initialized the object to be scanned is placed on the lower planar surface inside the rectangle defined by the fiducials. Any video camera or webcam can be used for image acquisition. The camera should looking in the scene from the front and slightly from the top (otherwise triangulation will result in large errors). The two lines of intersection between the laser plane and the planar boards and object slowly move across the screen in one direction (e.g. left to right), scanning the surface of the object. Each point on the object should be scanned carefully during data acquisition. The camera frame rate determines how fast the laser beam scans the surface so that enough frames are captured to obtain the resolution needed and avoid reconstruction artifacts. In the case of occlusion of parts of the object for the laser beam the scanning can be repeated with the laser source in a different angle and the resulting reconstructions can be combined at the end to overcome inclusion artifacts. The problem of occlusion is caused because parts of the object are partially hidden and therefore cannot be recognized robustly. Occlusion in the scene is considered as one of the principal sources of uncertainty. The occlusion can cause several problems, particularly the many false 2D points that appear when using edge detectors, consequently leading to the incorrectness of all further correspondences to images which contain those points [44].



Figure 26: Web-Camera used in the scanning procedure (*Microsoft Web LifeCam HD-3000*).



Figure 27: The black planes placed in 90° angle, with known fiducials and the checkerboard for the calibration stage.

The line-plane laser beam is achieved using a red laser pointer in combination of a cylindrical lens. In our case the cylindrical lens is used in order to shape the laser point source in a line-plane laser beam.

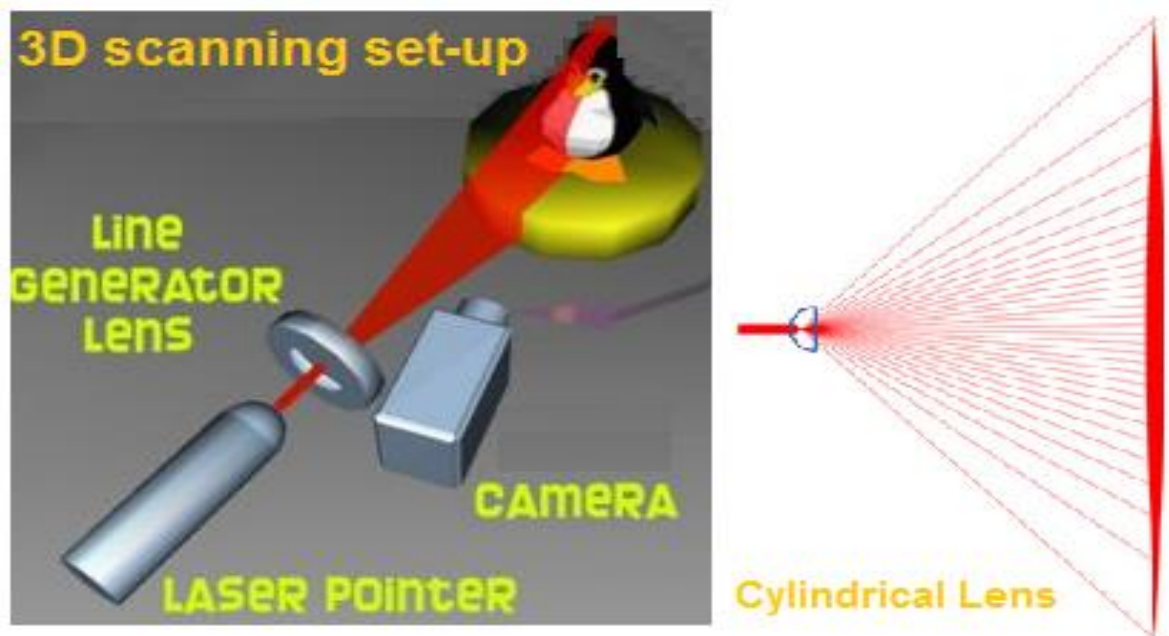


Figure 28: The usage of the cylindrical lens in the 3D scanning procedure.



Figure 29: Line-plane laser beam (scanning beam) and the components for the beam-shaping.

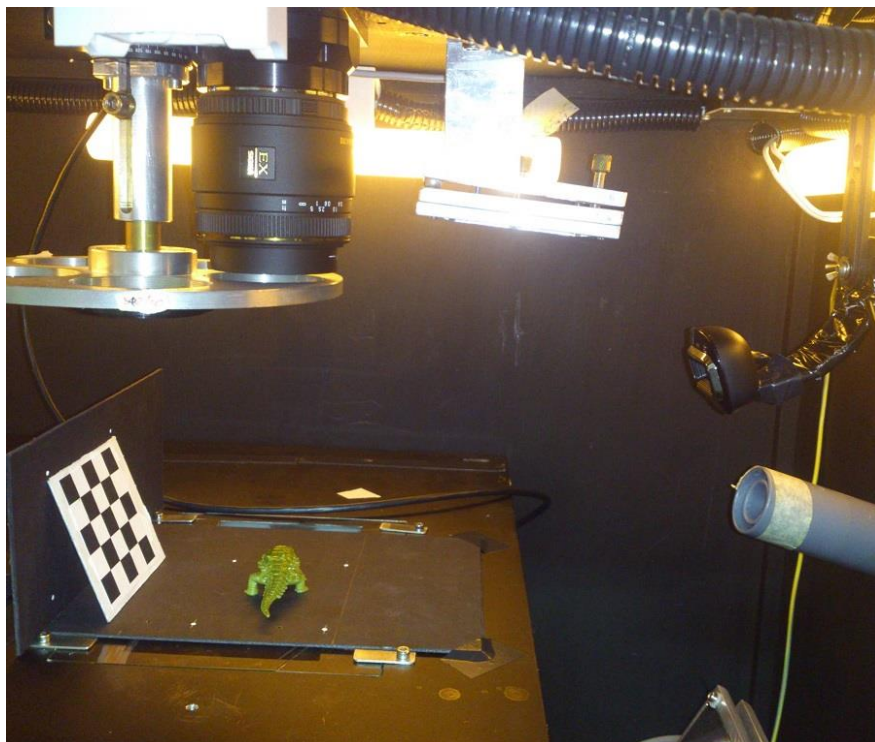


Figure 30: Adjustment of the process into the FMT System.

Results

As it is referred in the previous chapter, there are three main parts of the project. In the first part we are trying to determine the optical properties (μ_a, μ_s) of our specimens simulating the propagation of light inside the media using diffusion approximation. In the second part we use Kubelka-Munk model in order determine the optical characteristics of the materials that will be used for the final construction of the phantoms. Finally, we set-up a scanning procedure to obtain information about the shape of the object examined in order to use it as prior information in the forward/inverse model. Each part is done separately and the result are organized as follow:

1. Determination of optical characteristics of the material of the specimens used :

- a. Spectrophotometer Measurements,
- b. Kubelka- Munk Model

2. Simulation of the propagation of the light inside the media and determination of the optical properties (μ_a, μ_s) using diffusion approximation:

- a. FMT measurements,
- b. Forward Model (using Diffusion Equation) and
- c. Inverse Model

3. Scanning procedure for the 3D shape reconstruction of our sample:

- a. Camera Calibration procedure.
- b. Data acquisition.
- c. Image processing
- d. 3D reconstruction
- e. Adjustment in the FMT System.

5.1 Determination of optical characteristics of the material of the specimens used

As it is referred above, our specimens have cylindrical shape and their optical properties are determined using Kubelka-Munk model . The measurements of the parameters used in Kubelka-Munk are measured in Spectrophotometer in all spectra.

	<i>Tissue Type</i>	<i>Absorption coefficient</i> $\mu_a (mm^{-1})$	<i>Scattering coefficient</i> $\mu_s (mm^{-1})$
1	Brain	0.0191	6.6
2	Skull	0.0136	8.6
3	Skin	0.0186	11.1

Table 3: Absorption and scattering coefficients of each mouse's tissues that we are interested in. They were chosen from values given by the literature [13],[14], [39] and [http://mcx.sourceforge.net/cgi-bin/index.cgi?MMC/DigimouseMesh#Tissue_optical_properties]

The goal is to represent the optical properties of the mouse's head in a phantom as they are shown in the literature. In our work we don't take into account the CSF layer of the brain. In order to achieve the required optical parameters of the resin mixtures with the Kubelka-Munk approximation, cylindrical phantoms were made with a width of 1 mm and a diameter of 60mm. Two different groups of phantoms are used. In the first group black pigment is used as absorber while in the second group red pigment is used for the same reason. In each group white pigment is used as scattered. The concentrations are shown in the following table (Table 4). RTV silicone rubber (GLS- 50, Prochima) was used as casting material, which is consisted by two parts (part A, Part B) the silicone and its catalyst, both being liquids [38].

	C1			C2			C3			C4		
	1	2	3	1	2	3	1	2	3	1	2	3
Solution 1 (white pigment) (gr)	0,524	0,570	0,516	1,130	1,010	1,050	1,530	1,580	1,570	2,200	2,300	2,070
Solution 2 (black pigment) (gr)	0,235	0,205	0,223	0,210	0,220	0,240	0,230	0,230	0,200	0,200	0,260	0,240
Part A (gr)	2,168	2,457	2,423	1,926	1,959	0,998	1,430	1,461	1,480	0,960	0,920	1,195
Part B (gr)	1,882	1,921	1,963	1,890	2,500	1,960	2,170	2,040	1,900	2,650	2,070	2,050
Total (gr)	4,809	5,153	5,125	5,156	5,689	4,248	5,360	5,311	5,150	6,010	5,550	5,555
	C1			C2			C3			C4		
	1	2	3	1	2	3	1	2	3	1	2	3
White Pigment Concentration (w/w)	0,011	0,012	0,011	0,024	0,020	0,027	0,031	0,033	0,034	0,040	0,046	0,041
Black Pigment Concentration (w/w)	1,95 $\times 10^{-6}$	1,59 $\times 10^{-6}$	1,74 $\times 10^{-6}$	1,63 $\times 10^{-6}$	1,55 $\times 10^{-6}$	2,26 $\times 10^{-6}$	1,72 $\times 10^{-6}$	1,73 $\times 10^{-6}$	1,55 $\times 10^{-6}$	1,33 $\times 10^{-6}$	1,87 $\times 10^{-6}$	1,73 $\times 10^{-6}$
Mean Total Sum White Pigment concentration (w/w)	0,011			0,024			0,033			0,042		
Mean Total Sum Black Pigment concentration (w/w)	1,76 $\times 10^{-6}$			1,81 $\times 10^{-6}$			1,67 $\times 10^{-6}$			1,64 $\times 10^{-6}$		

Table 4: Samples with white and black pigment concentrations in order to test the Kubelka-Munk approximation, using spectrophotometer results.

In this group samples are measured twice in spectrophotometer in order to test repeatability and homogeneity.

	C1				
	1	2	3	4	5
Solution 1 (white pigment) (gr)	0,53	1,015	1,526	2,044	2,57
Solution 2 (red pigment) (gr)	0,22	0,22	0,2	0,22	0,24
Part A (gr)	2,58	1,986	1,47	0,954	0,53
Part B (gr)	1,97	1,89	1,93	1,89	2,02
Total (gr)	5,304	5,111	5,126	5,107	5,355
White Pigment Concentration (w/w)	0,011	0,022	0,033	0,044	0,053
Red Pigment Concentration (w/w)	0,000025	0,000026	0,000023	0,000026	0,000026

Table 5: Samples with white and red pigment concentrations in order to test the Kubelka-Munk approximation, using spectrophotometer results.

After the preparation of the tissue-like specimens, the samples are measured in the spectrophotometer in order to obtain diffuse reflectance and diffuse transmittance, which are the parameters that Kubelka-Munk model uses.

a. Spectrophotometer Measurements:

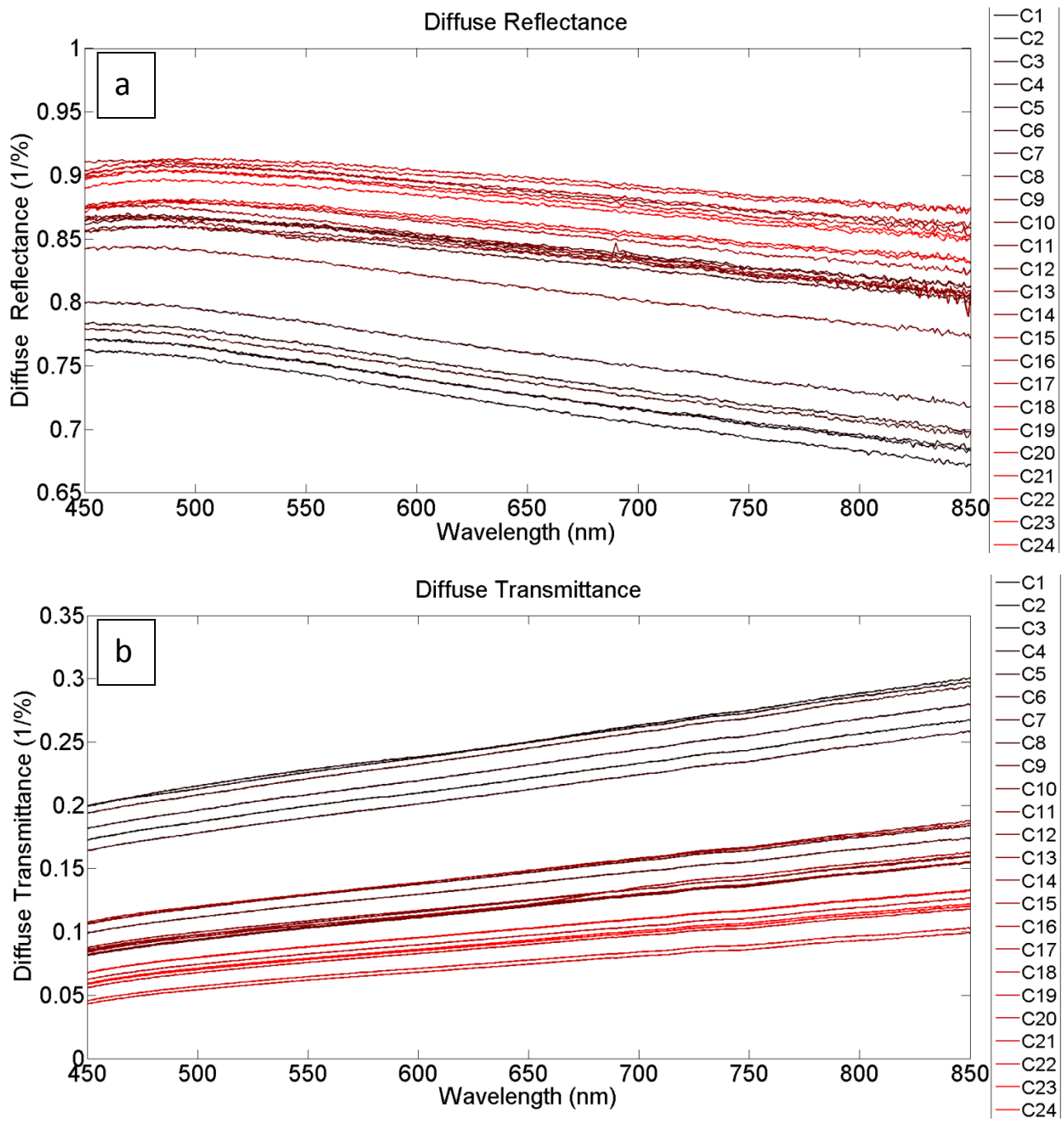


Figure 31: Diffuse Reflectance (a) and Diffuse Transmittance (b) vs. Wavelength. Measurements from Spectrophotometer. Samples with black and white pigment, width 1 mm and 60 mm diameter.

b. Kubelka-Munk results:

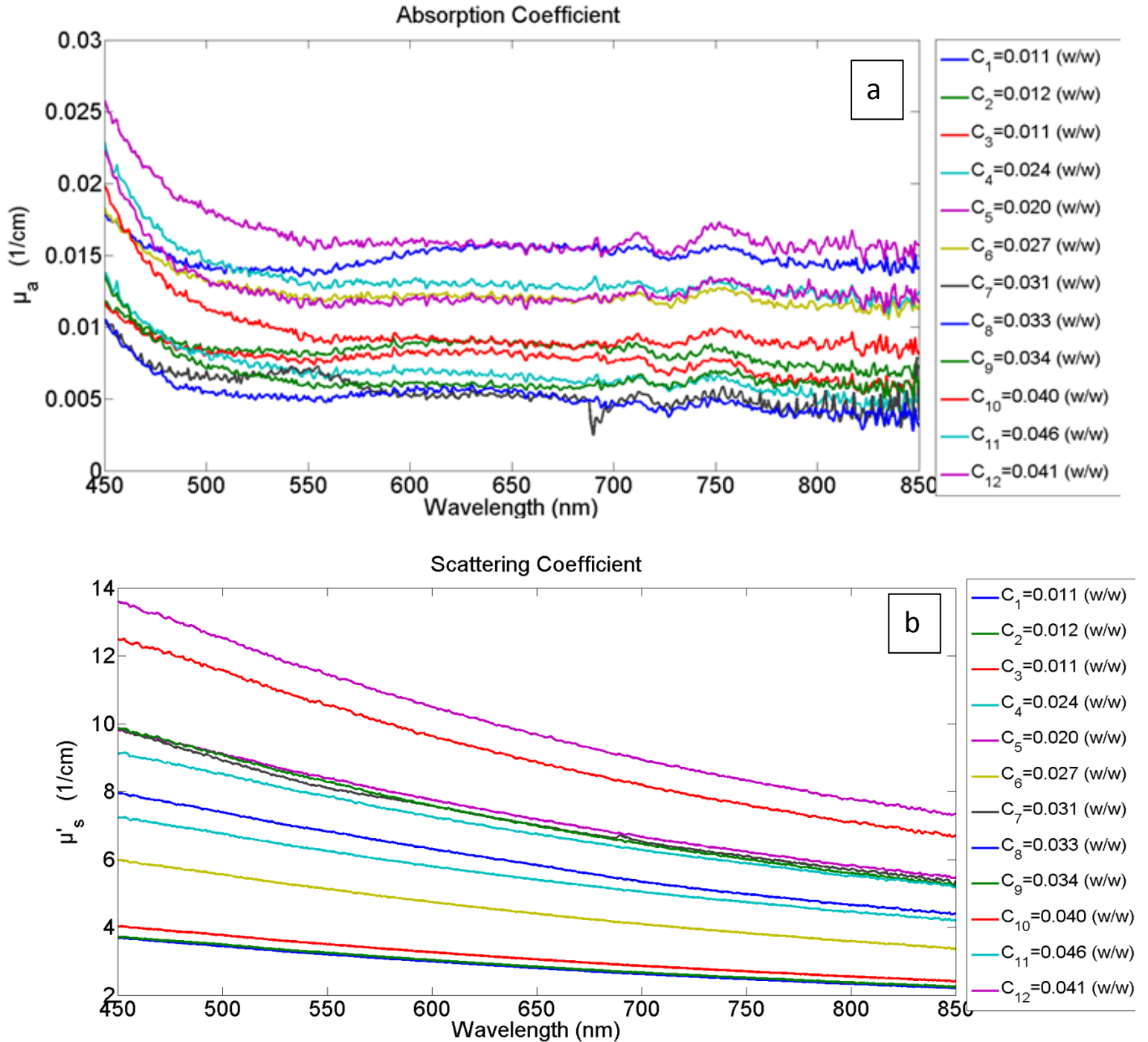


Figure 32: Absorption (μ_a) Coefficient (a) and Scattering (μ'_s) Coefficient (b) vs. Wavelength. Results from Kubelka-Munk calculations. Samples with black and white pigment, width 1 mm and 60 mm diameter.

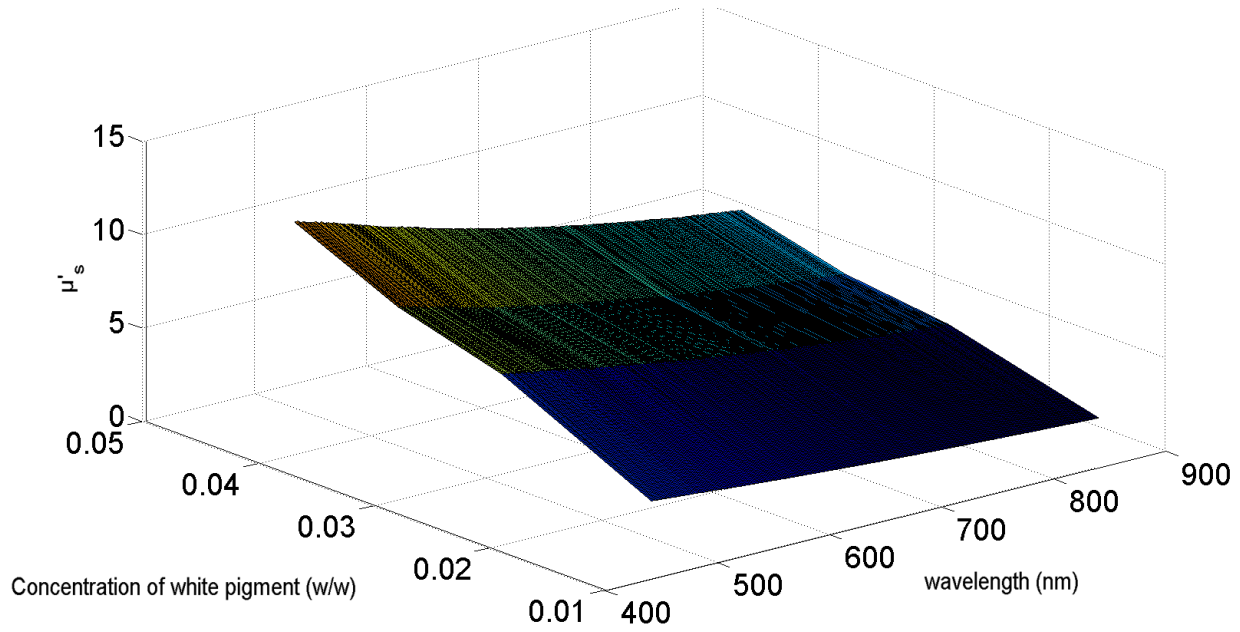


Figure 34: Scattering (μ'_s) coeff. Vs. Wavelength Vs. Concentration of white pigment (3D map).

5.2 Simulation of the propagation of the light inside the media and determination of the optical properties (μ_a, μ_s) using diffusion approximation

a. FMT measurements

For this part of the experiment simple, homogeneous and cylindrical specimens (19mm width and 60mm diameter) were created with unknown optical properties. These specimens were tested in the Fluorescent Molecular Tomography (FMT) system in four wavelengths: 458nm, 593nm, 635 nm, 685 nm. From the FMT system experiment a 512x 512 mm picture is obtained from the specimens. Data acquired from these measurements were used for the simulation of the propagation inside the media of specimens.

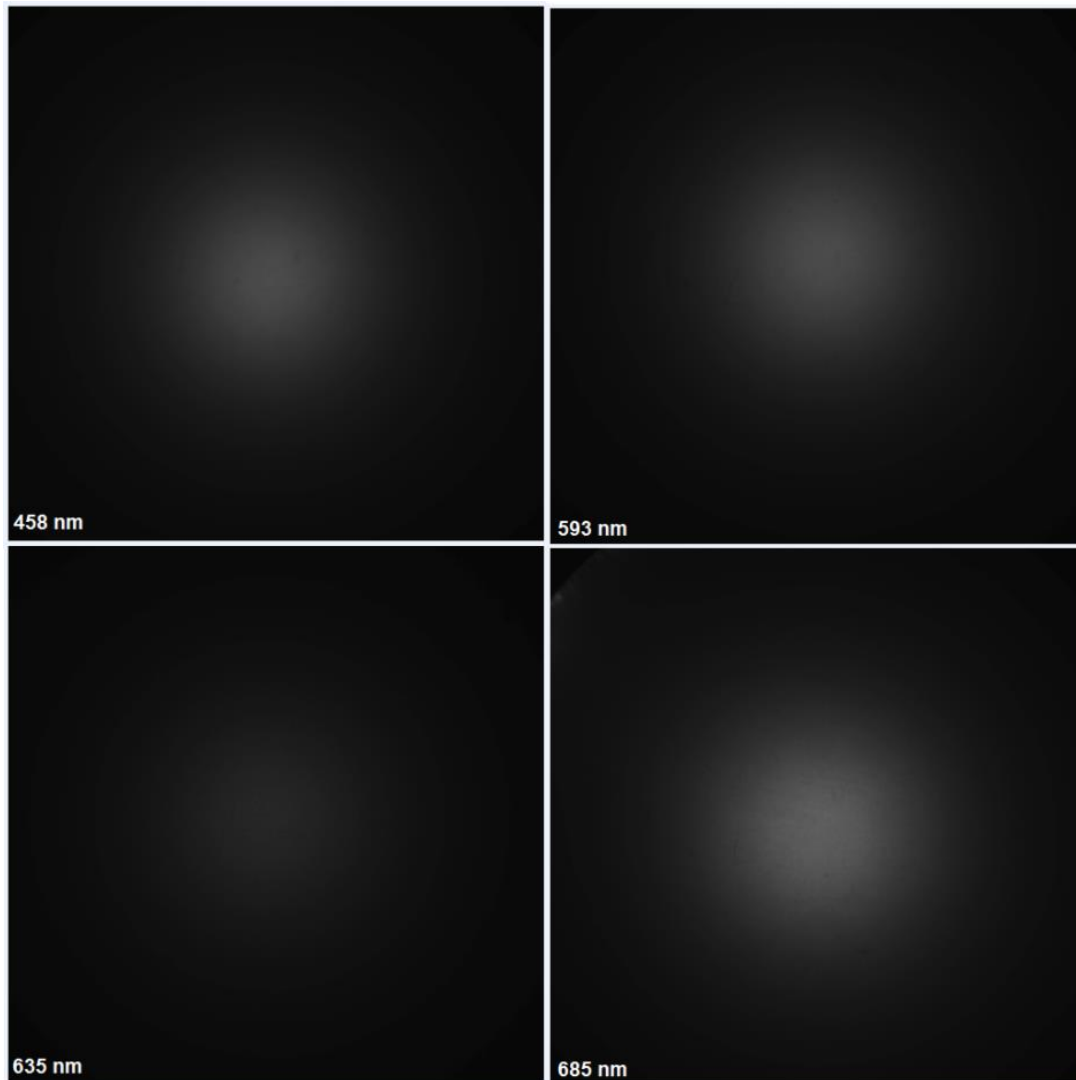


Figure 35: Data acquired from FMT system.

b. Forward Model (using Diffusion Equation)

To solve the forward problem cylindrical meshes are created to present the real shape of our specimens.

3D Cylindrical Mesh

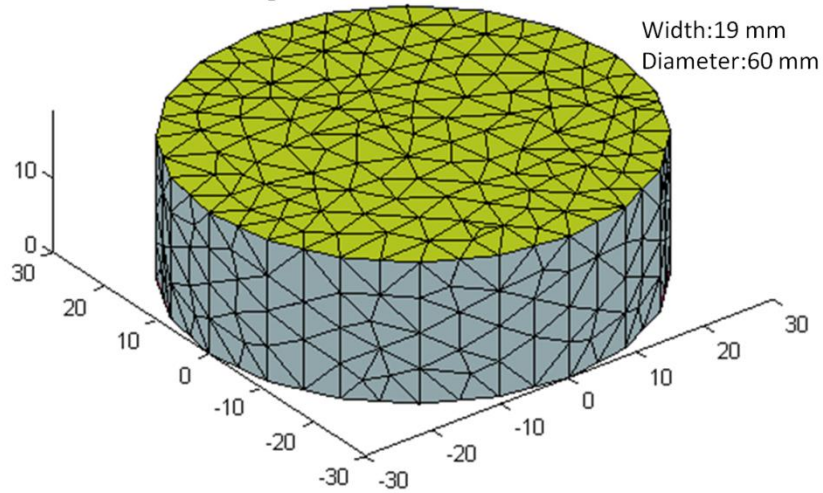


Figure 36: 3D Cylindrical Mesh. It represents the real domain of the phantom

The mesh represents the domain of the phantom which is the discretisation of the computation domain. It is composed of a list of node coordinates and a list of elements. The size of the Mesh is determined from the shape of the real geometry of the phantom. The next factor to describe the initial problem is to define the source. For that reason a clear cylindrical phantom was used. The source is usually a Gaussian distribution of light.

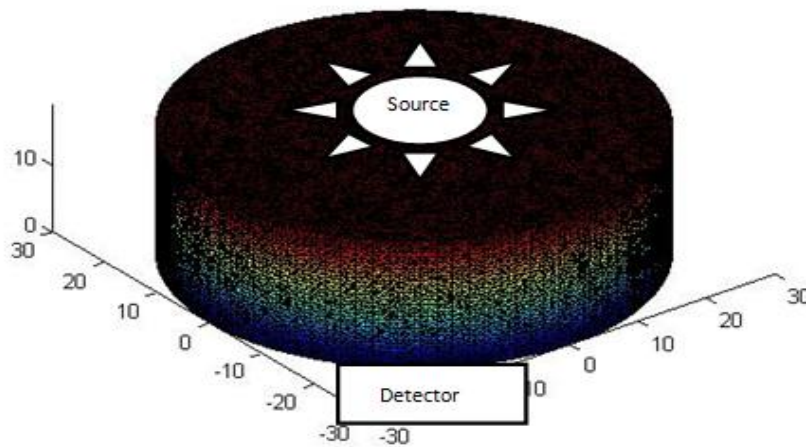


Figure 37: Definition of the source and the detector in the mesh.

In this point the cylindrical mesh must be aligned with the image. *Mapping* describes the correspondence of each pixel of the image on the surface of the mesh. The surface of the mesh must be scaled in order to fit the image.

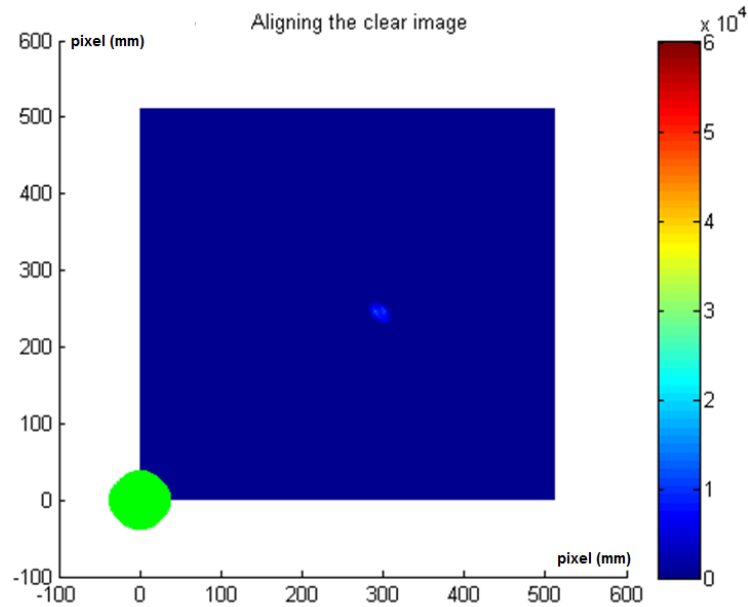


Figure 38: Green represents the surface (original size) of the mesh and the blue is the image (initial image) obtained from the FMT measurements

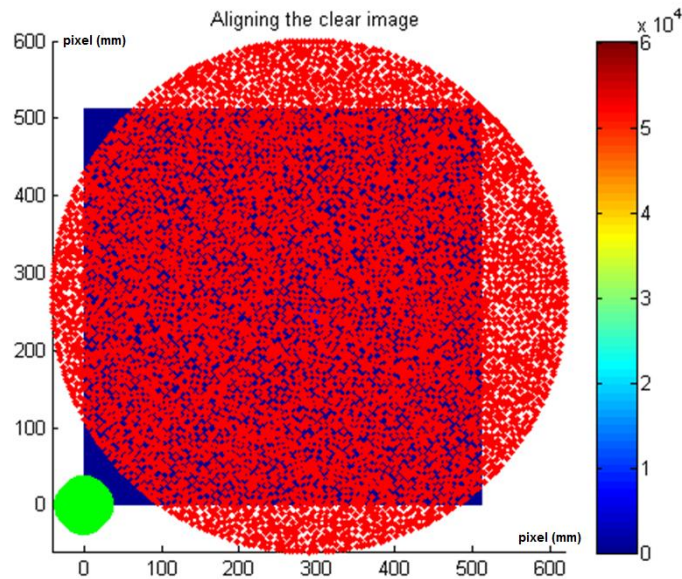


Figure 39: Scaling of the mesh surface in order to fit the initial image of the clear phantom. Red color represent the new surface of the mesh after scaling in order to have the center of the original image matched with the center of the mesh.

The initial image has integer number of pixels but the mesh has random number of nodes. This fact creates a restriction and therefore, a linear interpolation in the algorithm is followed in order to create the intermediate points, and have a total match between them.

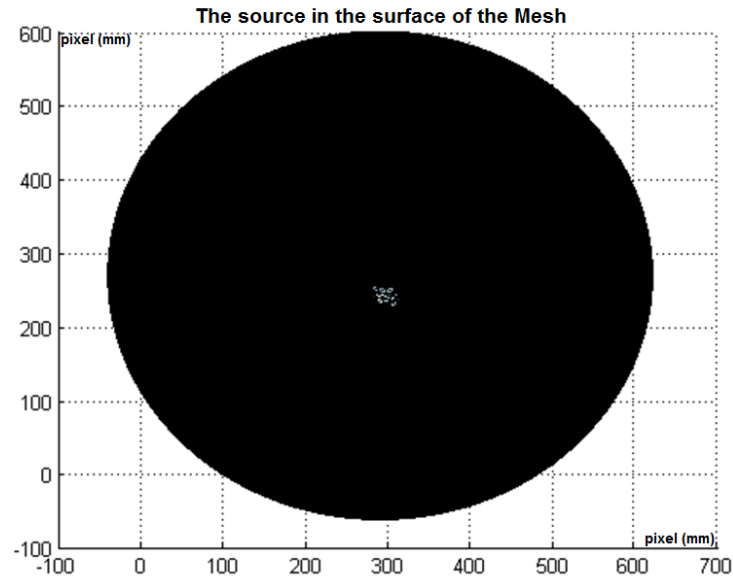


Figure 40: Image of the clear phantom after interpolation. In the center of the surface, the laser source is shown.

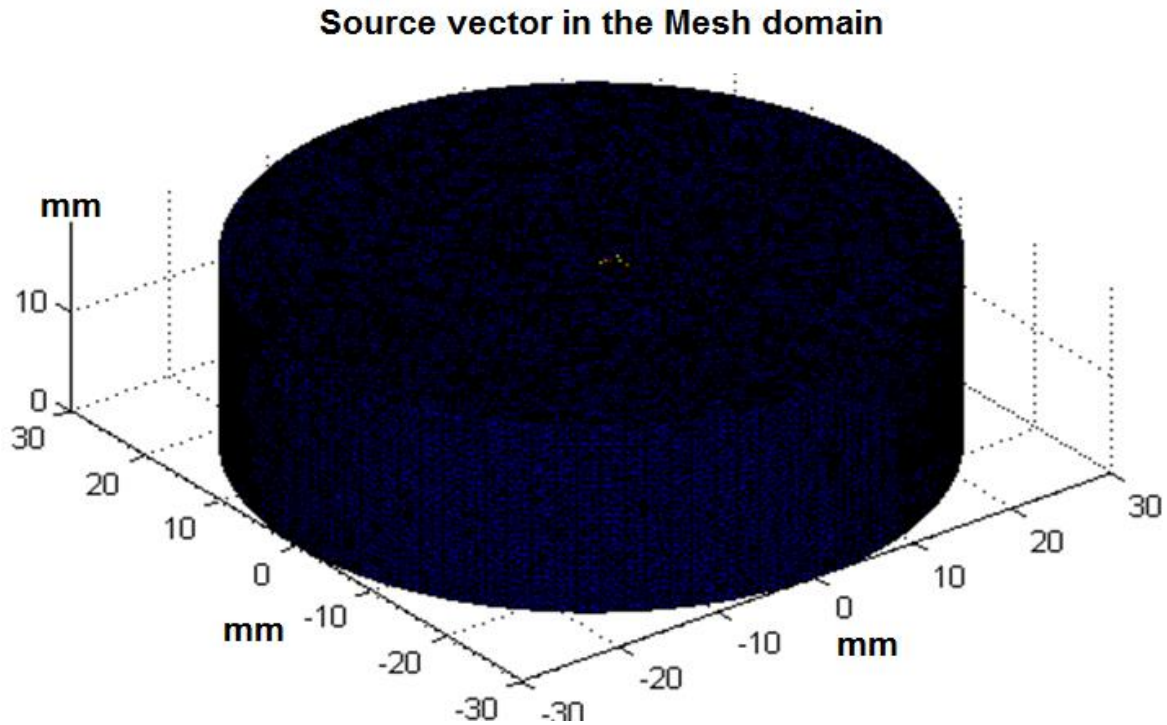


Figure 41: Data mapped in the Mesh domain.

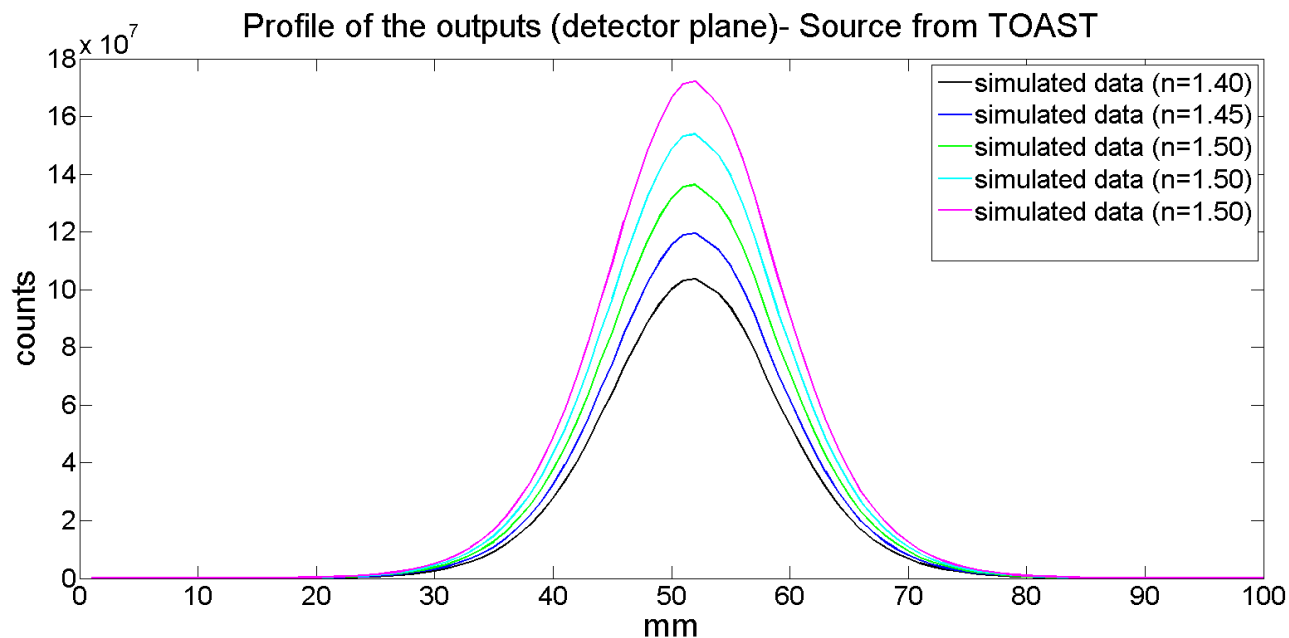


Figure 42: The Gaussian profile of the source (examples of TOAST Sources) on detector plane of the Mesh with different values of refractive index (n).

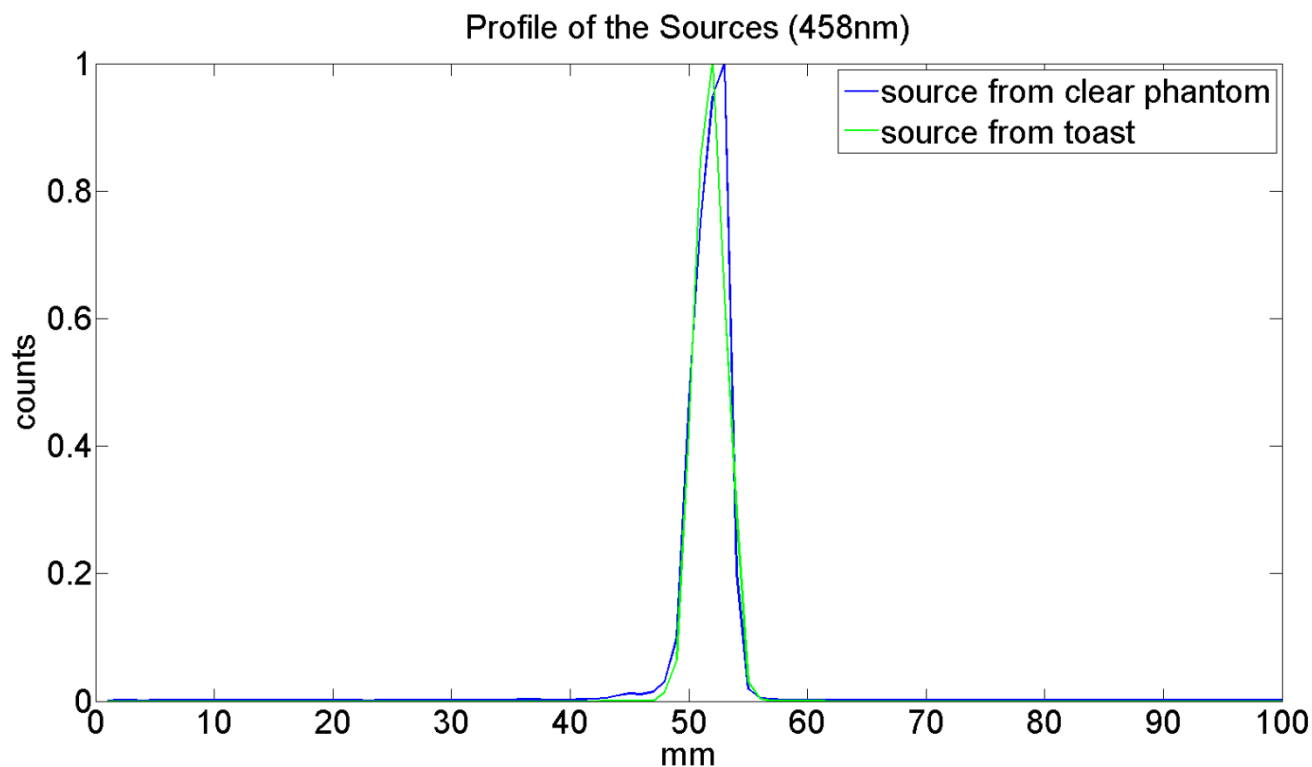


Figure 43: The comparison between the source from clear phantom and the source from Toast stimulation.

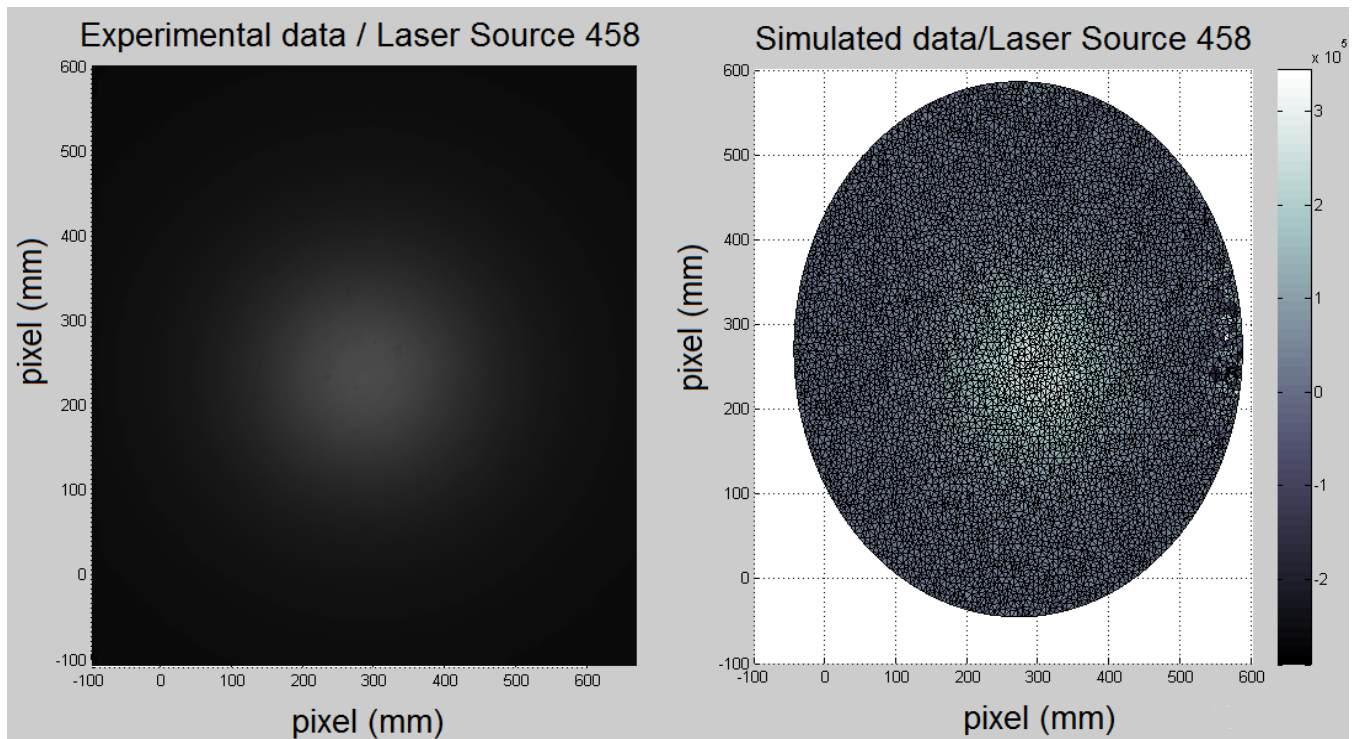


Figure 44: The simulation of the propagation inside the Mesh, based on the experimental set-up. Data are shown from the detector plane.

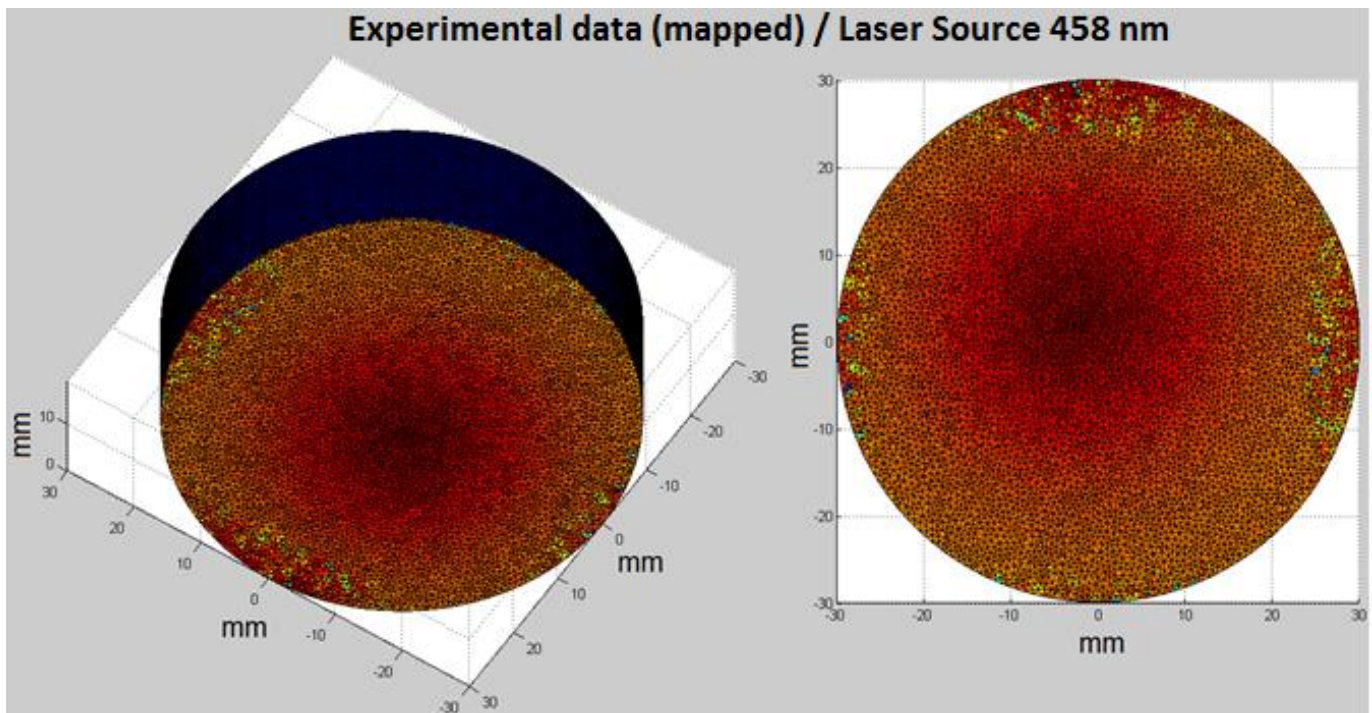


Figure 45: The mapping of the experimental data in the mesh surface.

c. Inverse Model

The final step in this section is a simple inverse mapping of actual measurements, so that modeled measurements match, as close as possible, the actual measurements. This is done by setting an objective function Ψ in order to compare the predicted and measured detector's readings. The optimization process is finished after the minimum of the objective function is found and the measured and predicted data match.

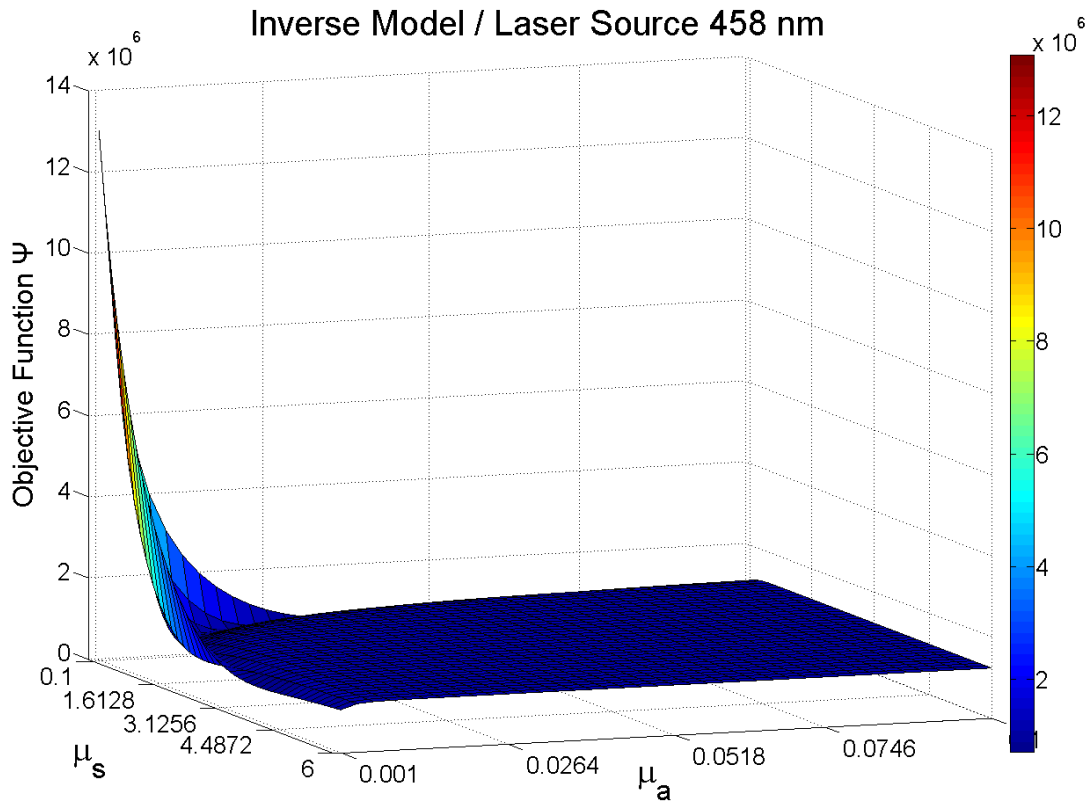


Figure 46: The solution of a simple inverse problem using an Objective function. When the minimum of the function Ψ is found, then the measured and the simulated data match. In the darkest color of blue is the minimum value of Ψ .

5.3 Scanning procedure for the 3D shape reconstruction of our sample

As it is referred in the previous paragraph, in this section the main parts of this procedure involve the following:

- Manually-assisted intrinsic camera calibration
- Manually-assisted extrinsic camera calibration
- 3D scanning with laser line plane
- Video capture using the Image Acquisition Toolbox

a. Camera Calibration procedure.

One aspect of camera calibration is to estimate the internal parameters of the camera. These parameters determine how the image coordinates of a point are derived, given the spatial position of the point with respect to the camera. The estimation of the geometrical relation between the camera and the scene is also an important aspect of calibration. The corresponding parameters that characterize such a geometrical relation are called external parameters. It is well known that actual cameras are not perfect and sustain a variety of aberrations. For geometrical measurements, the main concern is camera distortion, which relates to the position of image points in the image plane but not directly to the image quality. For example, the position of a point in a slightly blurred image can still be measured as the center of the blurred point. However, if the image position of a point is not accurate, the results that depend on its image coordinates will be erroneous.

Calibration images

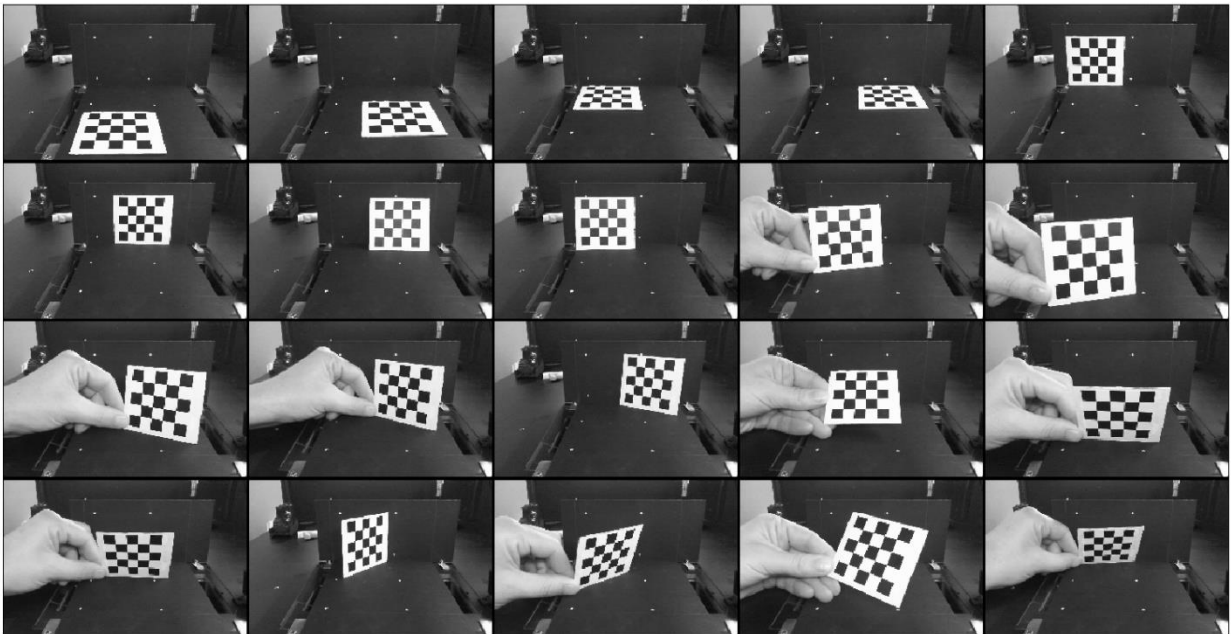


Figure 47: The positions of the calibration pattern in order to get the intrinsic and extrinsic parameters of the camera.

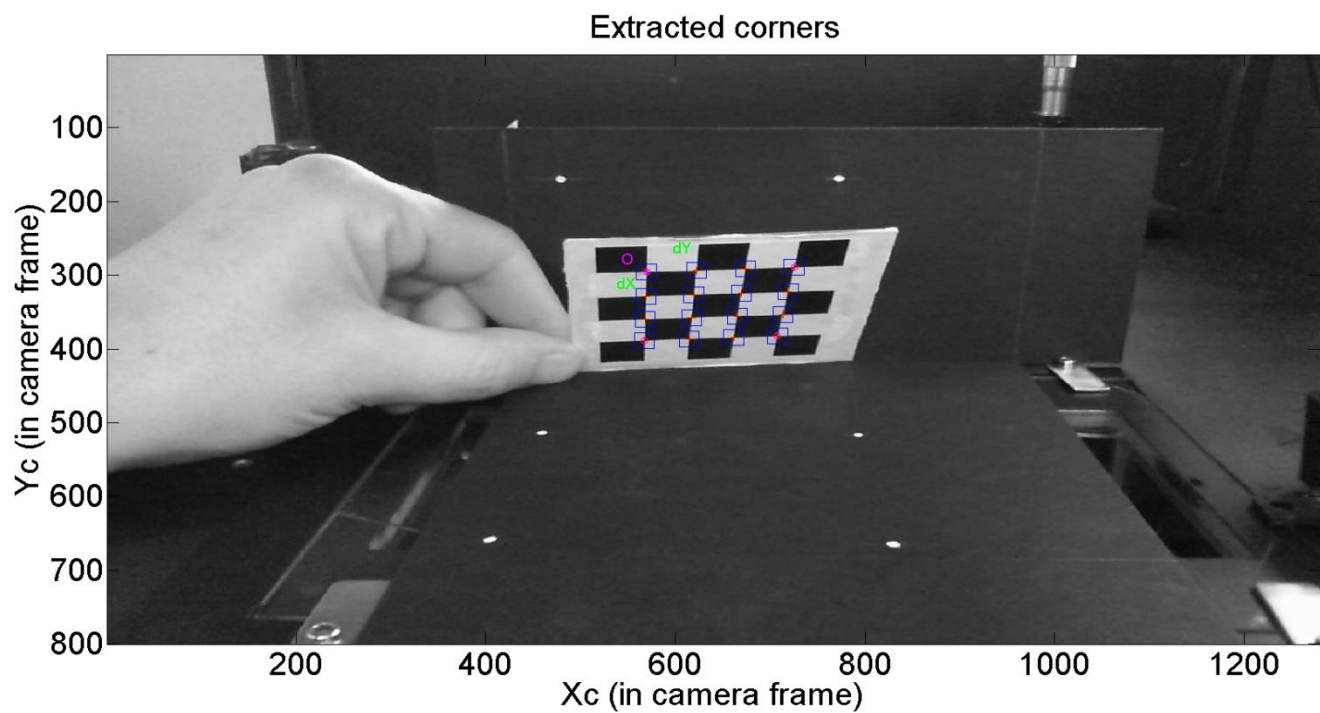


Figure 48: The extracted corners should match with the image corners.

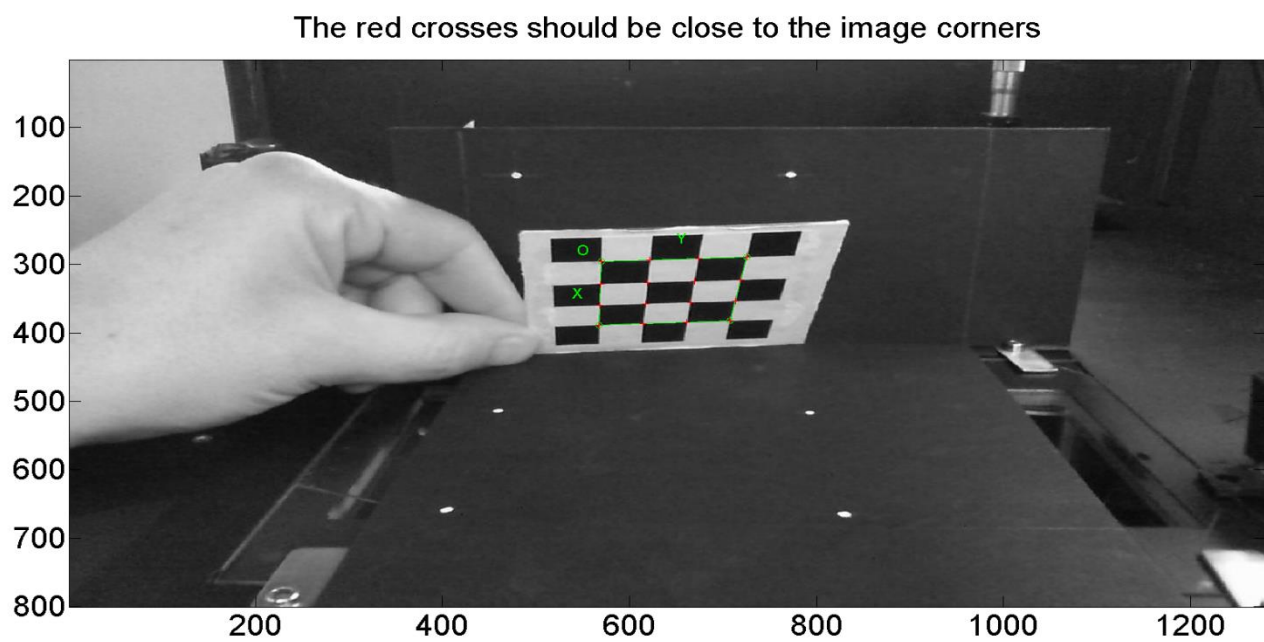


Figure 49: The extracted corners should match with the image corners.

Extrinsic parameters (camera-centered)

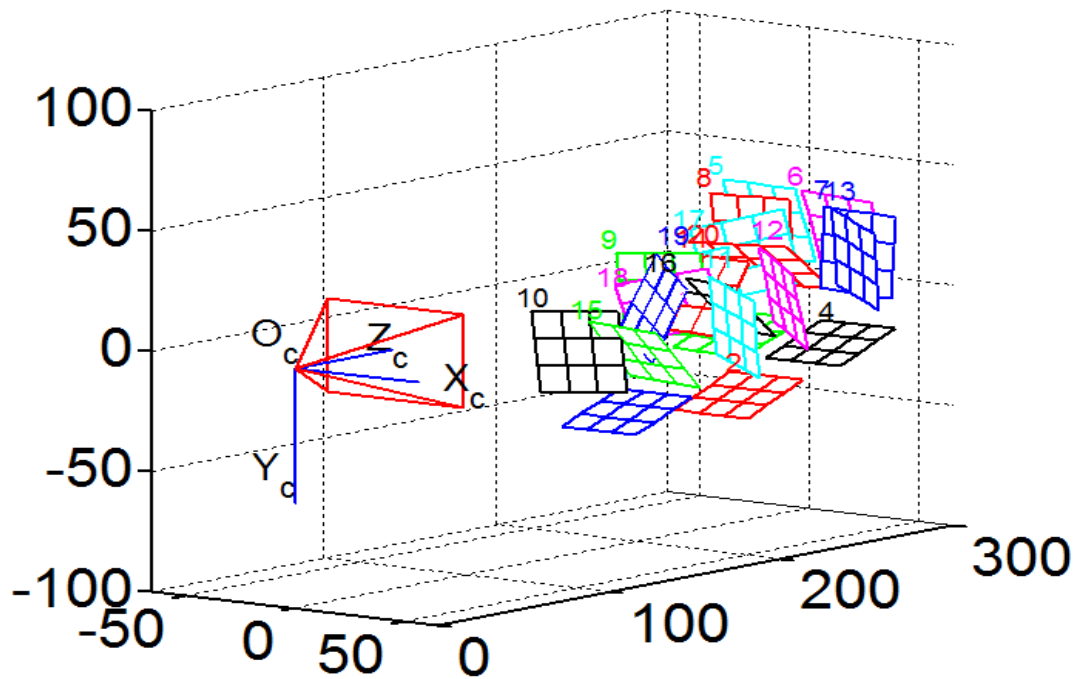


Figure 50: Extrinsic parameters of the camera (relative positions of the grids with respect to the camera). On this figure, the frame (O_c, X_c, Y_c, Z_c) is the camera reference frame. The red pyramid corresponds to the effective field of view of the camera defined by the image plane.

Calibration results (with uncertainties):

```
Focal Length:      fc = [ 1162.56399  1152.92874 ] ± [ 12.14616  12.34200 ]
Principal point:   cc = [ 605.18086   370.59299 ] ± [ 15.17775   16.95205 ]
Skew:             alpha_c = [ 0.00000 ] ± [ 0.00000 ]
                    => angle of pixel axes = 90.00000 ± 0.00000 degrees

Distortion:       kc = [ 0.14118  -0.82924  -0.01440  -0.00807  0.00000 ]
                    ± [ 0.04655   0.37461   0.00616   0.00555   0.00000 ]

Pixel error:      err = [ 0.11664  0.16511 ]
```

Figure 51: Intrinsic parameters of the camera.

The list of internal parameters [41],[42][43]:

- **Focal length:** The focal length in pixels is stored in the 2x1 vector **fc**.
- **Principal point:** The principal point coordinates are stored in the 2x1 vector **cc**.

- **Skew coefficient:** The skew coefficient defining the angle between the x and y pixel axes is stored in the scalar **alpha_c**.
- **Distortions:** The image distortion coefficients (radial and tangential distortions) are stored in the 5x1 vector **kc**.

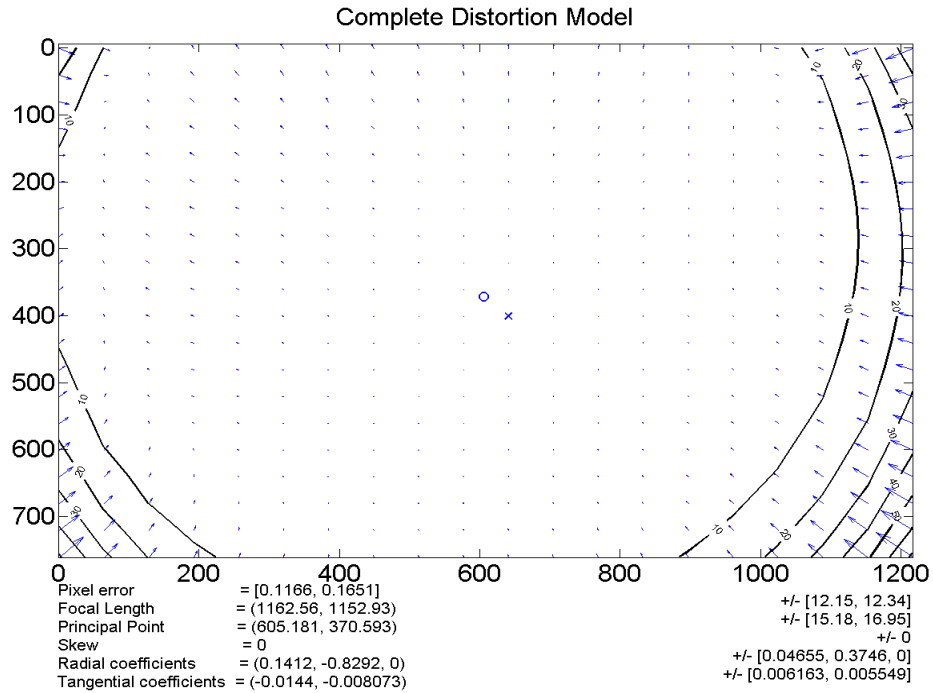


Figure 52(a): The distortion model on each pixel of the image.

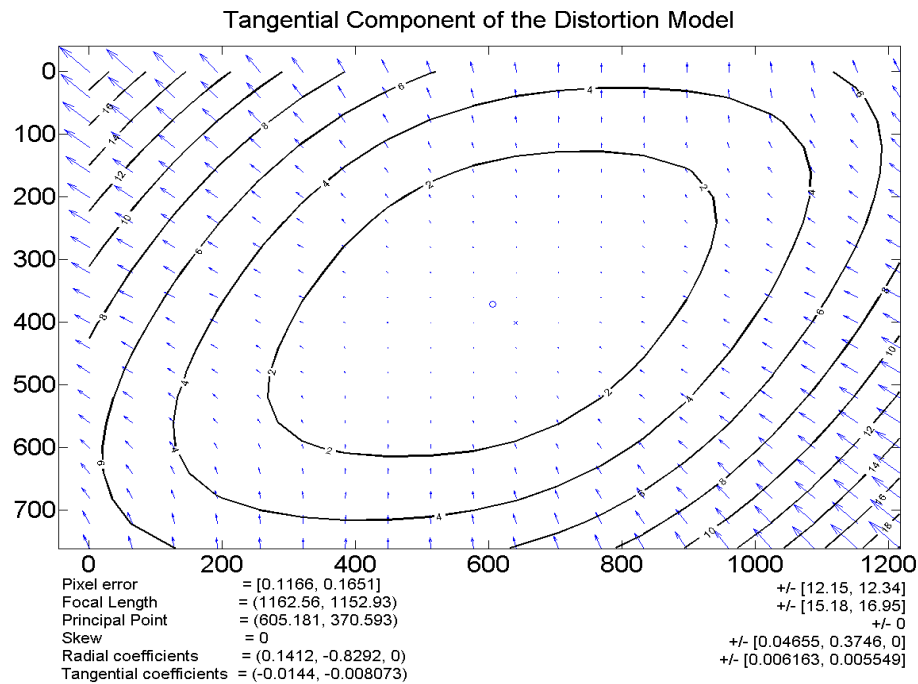


Figure 52(b): The distortion model (tangential) on each pixel of the image.

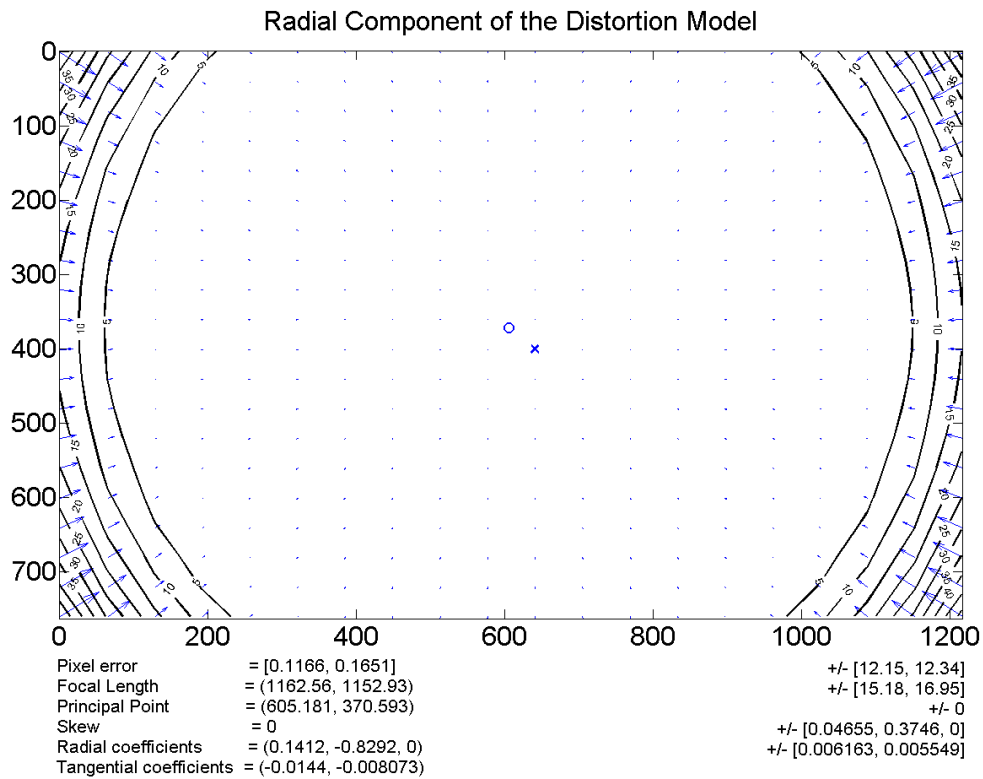


Figure 52(c): The distortion model (radial) on each pixel of the image.

The distortion model presents the geometrical distortion of the lens which concerns the position of image points in the image plane [45]. The figure 52(a) shows the impact of the complete distortion model (radial + tangential) on each pixel of the image. Each arrow represents the effective displacement of a pixel induced by the lens distortion. The figure 52(b) shows the impact of the tangential component of distortion. On this plot, the maximum induced displacement is 0.14 pixel (at the upper left corner of the image). Finally, the figure 52(c) shows the impact of the radial component of distortion. This plot is very similar to the full distortion plot, showing the tangential component could very well be discarded in the complete distortion model. On the three figures, the cross indicates the center of the image, and the circle the location of the principal point.

b. Data acquisition.



Figure 53: Data acquisitions and scanning procedure.

c. Image processing

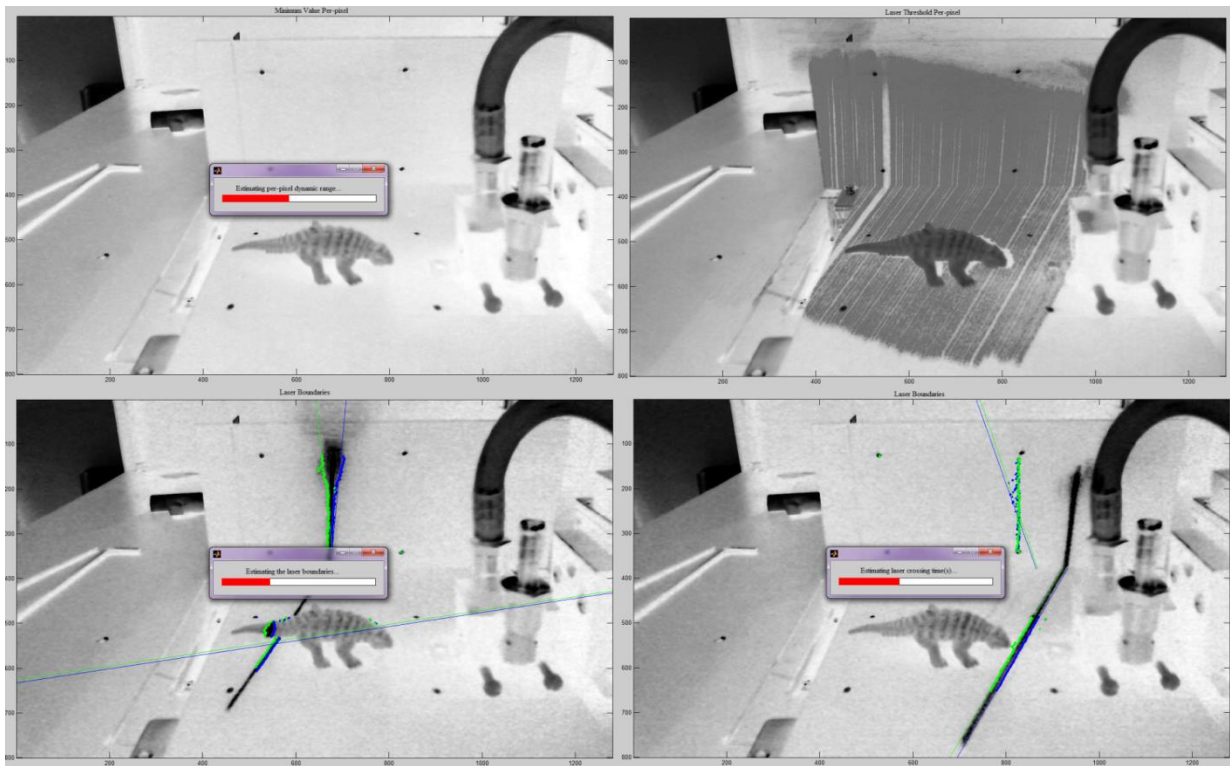


Figure 54: Performing Video Processing

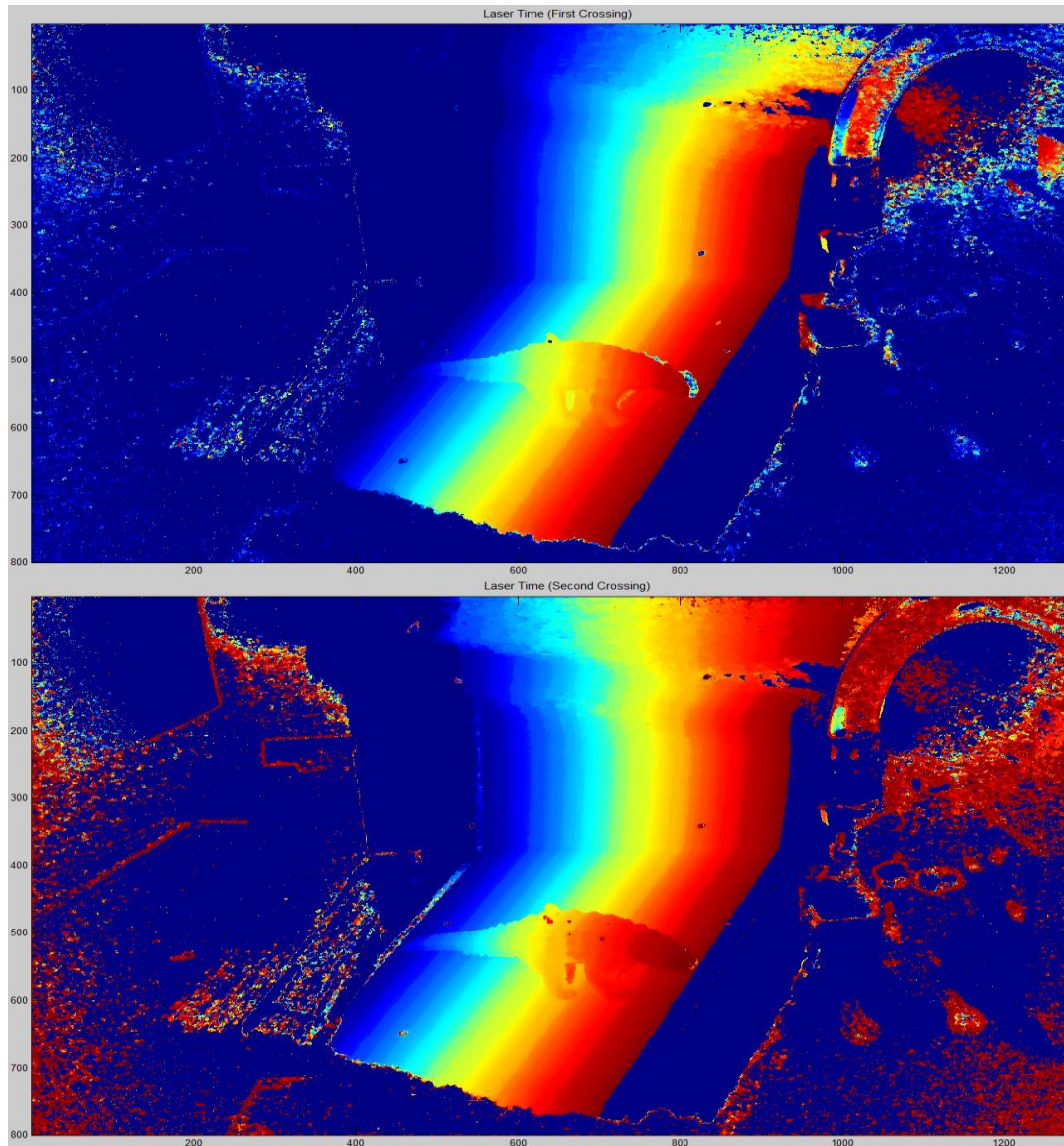


Figure 55: Performing Video Processing (2).

The video processing includes the localization of the dividing line between reference planes (horizontal calibration board from the vertical calibration board). The definition of the reference area for the "vertical" plane and "horizontal" plane is done with the presence of the fiducial point (white points in the boards). This procedure is done in order to automatically determine the position of the laser boundaries cast on each calibration board. Furthermore, the following procedures are also automatically estimated:

- The per-pixel dynamic range and laser beam thresholds,
- Laser beam boundaries,

- Laser beam crossing time(s).

The horizontal and vertical calibration planes position in the world coordinate system is done by clicking on the four fiducials on each plane, starting on the bottom-left and preceding counter-clockwise.

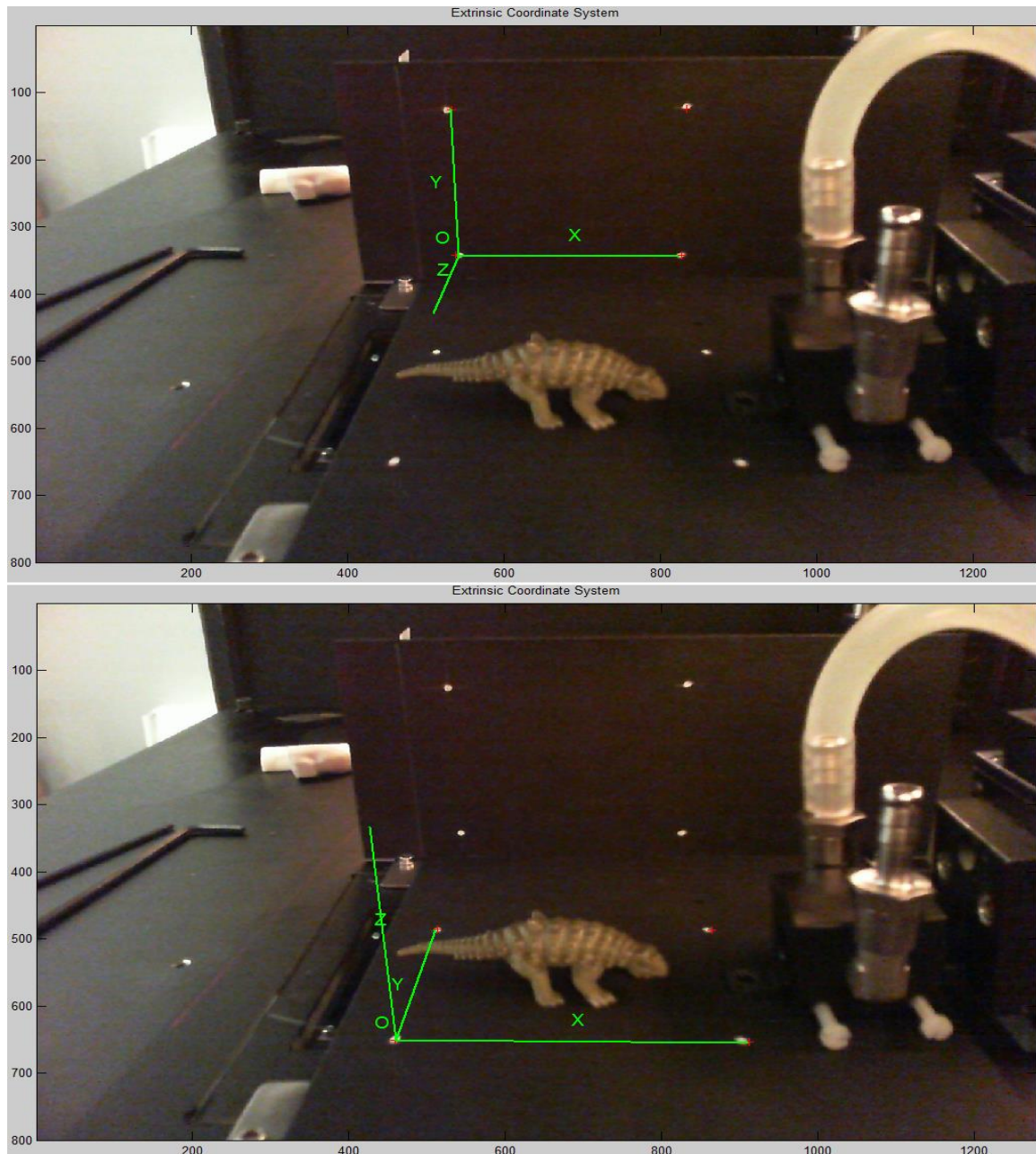


Figure 56: Performing Video Processing (3).

d. 3D point cloud reconstruction

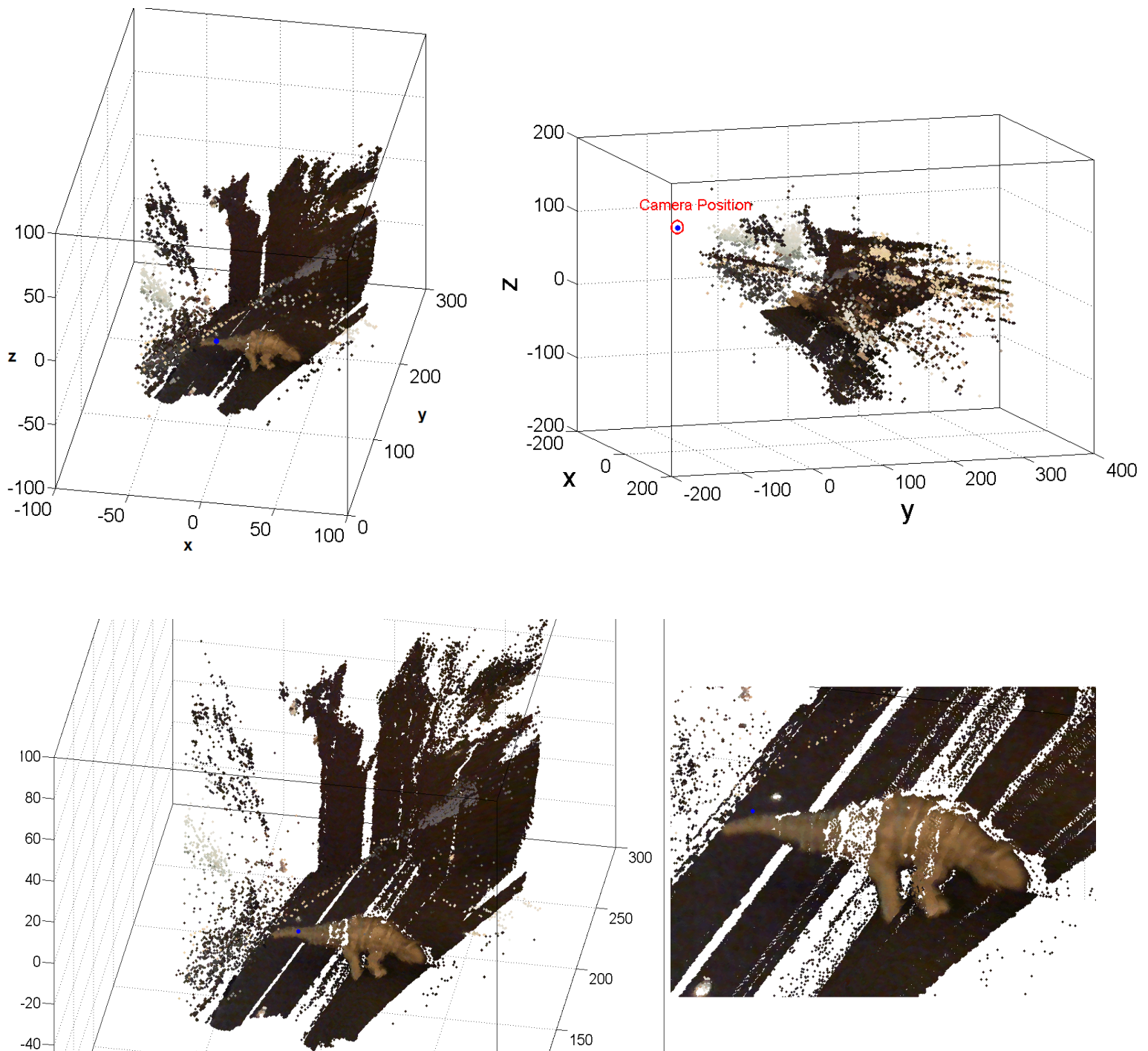


Figure 57: Reconstructed Point cloud.

e. Adjustment in the FMT System.



Figure 58: Adjustment of the components of scanning set-up in the FMT system.

6.1 Conclusion

As a conclusion, our work shows that using Diffusive Equation it is possible to describe the photon propagation of the light through the media. Also, solving the inverse problem the image reconstruction can be achieved. Adding prior information in forward and inverse model, it could be the solution to the problems that are caused from the highly diffusive nature of biological tissue which leads to restrictions in the resolution of the image (experimental data) as also in the accuracy of the quantification of the distribution of fluorescence targets inside the media. As is showed above, this prior information can be determined. Optical properties can be estimated using Kubelka-Munk model and the 3D shape of our sample can be reconstructed setting up a simple scanning procedure.

6.2 Future Work

Due to limited time the final goal of this project is not completed yet. The results showed in this work are part of the methodology to improve the FMT system and be used in future experiments. For having a better geometry representation there is still work to be done such as:

- Aligning the final 3D point clouds shape.
- Scanning the sample from different directions.
- Merging the different point cloud scans.
- Extracting polyhedral meshes from point clouds representations.
- Scanning the real head of the mouse.
- Solving the forward model given the 3D polyhedral mesh of the real head of the mouse.
- Solving the inverse in the given 3D polyhedral mesh of the real head of the mouse in order to achieve reconstruction of the fluorescence source distribution from measured light intensities.
- Comparing the optical properties obtained, for the same specimen, between Kubelka-Munk model and Diffuse Approximation (simulation procedure) .

References

1. Stuker F, Ripoll J, Rudin M: **Fluorescence molecular tomography: principles and potential for pharmaceutical research**. *Pharmaceutics* 2011, **3**(2):229-274.
2. Ntziachristos V: **Fluorescence molecular imaging**. *Annu Rev Biomed Eng* 2006, **8**:1-33.
3. Ntziachristos V, Culver JP, Rice BW: **Small-animal optical imaging**. *J Biomed Opt* 2008, **13**(1):011001.
4. Choy G, Choyke P, Libutti SK: **Current advances in molecular imaging: noninvasive in vivo bioluminescent and fluorescent optical imaging in cancer research**. *Mol Imaging* 2003, **2**(4):303-312.
5. Arridge SR: **Three-dimensional in vivo fluorescence diffuse optical tomography of breast cancer in humans**. *OPTICS EXPRESS* 2007.
6. Ripoll. J: **Principles of Diffuse Light Propagation: Light Propagation in Tissues With Applications in Biology and Medicine**. World Scientific Publishing 2012.
7. Wang LV, Wu H-i: **Biomedical optics : principles and imaging**. Hoboken, N.J.: Wiley ; Chichester : John Wiley [distributor]; 2007.
8. Joseph DK, Huppert TJ, Franceschini MA, Boas DA: **Diffuse optical tomography system to image brain activation with improved spatial resolution and validation with functional magnetic resonance imaging**. *Appl Opt* 2006, **45**(31):8142-8151.
9. Hall DJ, Hebden JC, Delpy DT: **Evaluation of spatial resolution as a function of thickness for time-resolved optical imaging of highly scattering media**. *Med Phys* 1997, **24**(3):361-368.
10. Ntziachristos V: **Going deeper than microscopy: the optical imaging frontier in biology**. *Nat Methods* 2010, **7**(8):603-614.
11. McCann CM, Waterman P, Figueiredo JL, Aikawa E, Weissleder R, Chen JW: **Combined magnetic resonance and fluorescence imaging of the living mouse brain reveals glioma response to chemotherapy**. *Neuroimage* 2009, **45**(2):360-369.
12. Raulin C, Karsai S: **Laser and IPL technology in dermatology and aesthetic medicine**. Berlin ; London: Springer; 2011.

13. Cheong WF, Prahl SA, Welch AJ: **A Review of the Optical-Properties of Biological Tissues.** *Ieee J Quantum Elect* 1990, **26**(12):2166-2185.
14. Jacques SL: **Optical properties of biological tissues: a review.** *Phys Med Biol* 2013, **58**(11):R37-61.
15. Fisher JC: **Photons, psychiatrics, and physicians: a practical guide to understanding laser light interaction with living tissue, part I.** *J Clin Laser Med Surg* 1992, **10**(6):419-426.
16. Jacques SL, Prahl SA: **Modeling optical and thermal distributions in tissue during laser irradiation.** *Lasers Surg Med* 1987, **6**(6):494-503.
17. Arnfield MR, Tulip J, McPhee MS: **Optical propagation in tissue with anisotropic scattering.** *IEEE Trans Biomed Eng* 1988, **35**(5):372-381.
18. Niemz MH: **Laser-tissue interactions : fundamentals and applications**, 2nd rev ed. edn. Berlin ; New York: Springer; 2002.
19. Driggers RG: **Encyclopedia of optical engineering.** New York: Marcel Dekker; 2003.
20. Boas DA: **Handbook of Biomedical Optics.** In.
21. Arridge SR: **Optical tomography in medical imaging.** *Inverse Probl* 1999, **15**(2):R41-R93.
22. Ishimaru A: **Wave propagation and scattering in random media.** New York: IEEE Press ; Oxford ; Oxford University Press; 1997.
23. Hussein EMA: **Computed Radiation Imaging Physics and Mathematics of Forward and Inverse Problems;** 2011.
24. **Optical tomography in the presence of void regions.** 2000.
25. Lin Y, Gao H, Nalcioglu O, Gulsen G: **Fluorescence diffuse optical tomography with functional and anatomical a priori information: feasibility study.** *Physics in medicine and biology* 2007, **52**(18):5569-5585.
26. Guven M, Yazici B, Intes X, Chance B: **Diffuse optical tomography with a priori anatomical information.** *Physics in medicine and biology* 2005, **50**(12):2837-2858.
27. Arridge SR, Hebden JC: **Optical imaging in medicine: II. Modelling and reconstruction.** *Physics in medicine and biology* 1997, **42**(5):841-853.
28. Hebden JC, Arridge SR, Delpy DT: **Optical imaging in medicine: I. Experimental techniques.** *Physics in medicine and biology* 1997, **42**(5):825-840.
29. Zacharopoulos AD, Svenmarker P, Axelsson J, Schweiger M, Arridge SR, Andersson-Engels S: **A matrix-free algorithm for multiple wavelength fluorescence tomography.** *Opt Express* 2009, **17**(5):3025-3035.

30. Schweiger M, Arridge S: **The Toast++ software suite for forward and inverse modeling in optical tomography.** *J Biomed Opt* 2014, **19**(4):040801.
31. Schweiger M, Arridge SR: **The finite-element method for the propagation of light in scattering media: frequency domain case.** *Medical physics* 1997, **24**(6):895-902.
32. Wai Gung Cheong, Scott A. Prahl, Ashley J. Welch: **A review of optical properties in biological tissues.** *IEEE Journal of Quantum Electronics* December 1990, **26**(12).
33. Krainov AD, Mokeeva AM, Sergeeva EA, Agrba PD, Kirillin MY: **Optical properties of mouse biotissues and their optical phantoms.** *Optics and Spectroscopy* 2013, **115**(2):193-200.
34. Douglas Lanman, Gabriel Taubin, **Build Your Own 3D Scanner**, SIGGRAPH 2009 Course Notes.
35. O. Faugeras: **Stratification of 3-D vision: projective, affine, and metric representations.** *Journal of the Optical Society of America* 1995., **12**(3):465–484.
36. Zhang Z.: **Determining the Epipolar Geometry and its Uncertainty: A Review.** *The International Journal of Computer Vision* 1998, **27**(2):161–195.
37. Zhang Z.: **Flexible Camera Calibration by Viewing a Plane from Unknown Orientations.** In *Proc. 7th International Conference on Computer Vision, Kerkyra, Greece*, pages 666–673, September 1999.
38. Avtzi S.: **Fabrication and characterization of a 3-D non-homogeneous tissue-like mouse phantom for optical imaging,** Undergraduate Thesis, Faculty of Science and Engineering Department of Physics University of Crete, May 2014, Herakleio, Crete.
39. Dogdas B., Stout D., Chatziioannou A. F. and Leahy R. M., **Digimouse: a 3D whole body mouse atlas from CT and cryosection data.** *Phys Med Biol* 2007, **52**(3): 577-87.
40. <http://www.perkinelmer.com>.
41. http://www.vision.caltech.edu/bouguetj/calib_doc/htmls/example.html
42. Heikkilä J. and Silvén O.: **A Four-step Camera Calibration Procedure with Implicit Image Correction,** Infotech Oulu and Department of Electrical Engineering University of Oulu.
43. http://www.vision.caltech.edu/bouguetj/calib_doc/htmls/parameters.html
44. Peiravi A., Taabbodi B.: **A Reliable 3D Laser Triangulation-based Scanner with a New Simple but Accurate Procedure for Finding Scanner Parameters,** *Journal of American Science* 2010, **6**(5):80-85.

45. Weng J., Cohen P., Herniou M.: **Camera Calibration with Distortion Models and Accuracy Evaluation**, *IEEE Transactions on Pattern Analysis and Machine Intelligence* 1992, 14(10): 965-980
46. Hielschera A.H., Bluestone A.Y., Abdoulaev G.S., Klose A.D., Lasker J., Stewart M., Netz U., Beuthan J.: **Near-infrared diffuse optical tomography**, *Disease Markers*, IOS Press 2002, 18(5-6): 313-337.
47. <http://www.mpoweruk.com/radio.htm>
48. <http://www.quora.com/What-is-the-Jablonski-diagram>
49. <http://www.olympusmicro.com/primer/lightandcolor/fluoroexcitation.html>
50. http://www.nature.com/icb/journal/v88/n4/fig_tab/icb2009116f1.html
51. http://guides.archaeologydataservice.ac.uk/g2gp/LaserScan_1-2
52. <http://www.david-lazerscanner.com/>